aerospace

MDPI

Article

Attitude–Trajectory Optimization for Low-Detectability Spacecraft Proximity Operations with Multiple Spacecraft Observers

Jixing Li, Chao Zhang, Bin Nan and Shunli Li *

School of Astronautics, Harbin Institute of Technology, Harbin 150001, China; lijixinghit@163.com (J.L.)
* Correspondence: lishunli@hit.edu.cn

Abstract

To address the trajectory detours and increased control effort that can arise from field-of-view (FOV) avoidance schemes in environments containing multiple third-party observing spacecraft, this paper investigates joint attitude–trajectory planning for geometry-based low-detectability proximity operations of a spacecraft with unidirectional main thrust. A coupled attitude–trajectory optimal control model with multiple constraints is established by considering a fixed forward-looking camera, a rear propulsion aperture, direction-dependent solar-array geometric blocking, and unidirectional main thrust. Compound state-triggered constraints (cSTCs) are used to describe the direction-dependent low-detectability geometric requirements activated within third-party observation FOVs, and the resulting problem is solved within a successive convexification (SCvx) framework. In the main case, all FOV-active transcription nodes of the attitude-assisted solution satisfy the prescribed direction-dependent geometric constraints. Compared with the FOV-avoidance scheme, the attitude-assisted scheme reduces the thrust impulse by 45.35% in the considered main scenario. In a scenario in which the terminal location is unavoidably inside a third-party observation FOV, the attitude-assisted formulation admits a discrete solution by adjusting the direction-dependent low-detectability geometry, illustrating the additional mission-design freedom provided by attitude assistance for the specific terminal-covered geometry considered in this study.

Keywords: spacecraft proximity operations; stealth attitude planning; unidirectional thrust; compound state-triggered constraints; successive convexification

1. Introduction

With the continuing advancement of space situational awareness (SSA), the orbital states and mission activities of on-orbit spacecraft are subject to increasingly persistent and detailed observation. Existing space-object surveillance systems mainly comprise ground-based radar, ground-based electro-optical systems, and space-based optical systems. Ground-based systems offer advantages in aperture and power but are limited by geographical deployment, Earth occultation, and atmospheric conditions. Space-based observing platforms can expand their surveillance coverage through orbital motion and obtain high spatial resolution at close range, thereby providing an important complement to ground-based surveillance [1,2]. Therefore, when performing proximity operations, inspection, and formation-flying missions, a spacecraft may need not only to satisfy conventional requirements concerning safety, fuel, and terminal states but also to reduce the risk

Check for updates

Academic Editor: Stefano Silvestrini

Received: 28 August 2026
Revised: 30 September 2026
Accepted: 13 October 2026
Published: 16 October 2026

Copyright: © 2026 by the authors. Licensee MDPI, Basel, Switzerland. This article is an open access article distributed under the terms and conditions of the Creative Commons Attribution (CC BY) license.

of continuous tracking of its trajectory and mission activities by third-party observation systems. This need gives rise to the problem of spacecraft covert-maneuver planning.

Covert spacecraft maneuvers are generally achieved by actively designing the spacecraft motion states and relative geometric relationships so that a mission spacecraft reduces its exposure to space-object surveillance systems while satisfying orbital dynamics and mission boundary conditions [2]. Existing studies first focused on surveillance avoidance at the trajectory level. Wang et al. [3] used changes in the relative positions of a spacecraft swarm to construct internal occultation relationships and employed a geodesic method to plan swarm trajectories satisfying dynamics, collision-avoidance, and covert-configuration constraints. Tang et al. [4] further used an affine-geodesic method to address nonlinear relative dynamics and covert maneuvers with multiple constraints. Zheng et al. [5] constructed FOV constraints from the optical-sensor FOVs of observing spacecraft and planned spacecraft-swarm trajectories around the observation regions to achieve covert maneuvers under fixed and rotating sensor conditions. When the surveillance regions are relatively sparse, these methods can effectively exploit spatial geometric freedom to obtain covert trajectories. However, as the number of surveillance platforms increases and observation regions become contiguous or overlapping, orbital maneuvers alone may have difficulty continuously avoiding space-object surveillance systems.

In addition to actively avoiding detection by changing the trajectory, reducing the observable signatures of the spacecraft itself is another important means of improving on-orbit low-detectability. Existing studies have investigated low-observable spacecraft design in terms of external configuration, materials, and related aspects and have obtained favorable low-observable performance [6–8]. The associated simulations and experiments also show that the radar cross-section (RCS) of a spacecraft is strongly direction-dependent and is closely related to the observer's direction relative to the spacecraft body. Consequently, a low-observable configuration can generally maintain favorable scattering characteristics within a limited range of observation angles. This directional dependence has also been studied in the field of low-observable aircraft. Lu et al. [9] indicated that RCS peaks and their exposure durations in different incident directions can substantially affect radar-detection probability. Guan et al. [10] showed from the maneuver-mechanism perspective that relative-attitude changes induced by roll during turning may cause an aircraft to re-enter a high-RCS angular region.

Su [11] performed active attitude planning based on the RCS, orbital position, and radar-threat direction of a microsatellite, orienting its low-RCS direction toward the principal threat region to reduce the risk of radar detection during on-orbit operation. Hua et al. [12] further considered multisource detection by ground-based, sea-based, and space-based systems and studied microsatellite attitude optimization based on directional low-RCS characteristics under complex attitude constraints. More recently, Li et al. [13] developed an attitude planning and control framework directly on $SO(3)$ for flexible spacecraft subject to attitude-forbidden regions, combining an $SO(3)$-based RRT* planner with prescribed-performance control. However, existing low-observable attitude planning and spacecraft covert-trajectory planning remain largely separate. The former generally optimizes a low-RCS orientation with a prescribed orbit or flight path, without treating orbital motion as a simultaneous decision variable. The latter mainly avoids observation regions by changing the spacecraft position trajectory or relative formation configuration and seldom exploits the spacecraft's own direction-dependent low-detectability characteristics. If a low-detectability servicing spacecraft is designed to minimize exposed propulsion apertures and to concentrate its main propulsion along a single body-fixed direction, the translational thrust vector must be redirected through attitude maneuvers. Meanwhile, the forward-looking camera in a proximity mission must maintain continuous observation of

the target. Target imaging, low-detectability orientation, attitude motion, and translational control therefore exhibit pronounced 6-DOF coupling and pose a challenge to spacecraft planning algorithms.

For an autonomous approach to a noncooperative target, Chen et al. [14] used an improved RRT* algorithm and a "rotate–fire–rotate again" strategy to construct a real-time integrated guidance-and-control framework for an underactuated microsatellite, providing a sampling-based approach to joint attitude–trajectory planning under collision-avoidance, camera-FOV, and single-thruster executability constraints. Recent work by Wei et al. [15] formulated a nonlinear optimal control problem for spacecraft rendezvous and docking under force, velocity, field-of-view, and collision-avoidance constraints and solved it using a symplectic numerical method. For spacecraft optimal control problems involving nonlinear dynamics, control constraints, and nonconvex path constraints, convex-optimization-based trajectory-generation methods have become an important approach to spacecraft trajectory optimization because of their computational efficiency and constraint-handling capability [16]. Liu and Lu [17] solved nonconvex optimal control problems using sequential convex programming. On this basis, to alleviate artificial infeasibility and local-model distortion caused by linearization, Mao et al. proposed successive convexification (SCvx), introducing virtual control and slack variables into the convex subproblem and combining them with trust region updates to maintain the feasibility of successive iterations [18]. They subsequently extended this framework to optimal control problems with nonconvex state constraints [19]. Zhou et al. [20] applied sequential convex programming to an autonomous approach toward a noncooperative target while considering coupled attitude–trajectory dynamics, camera FOV, and collision-avoidance constraints for the target spacecraft body and solar arrays. Zhang et al. [21] further applied sequential convex programming to autonomous rendezvous-and-docking trajectory optimization involving 6-DOF dynamics and complex path constraints. Building on these studies, this paper investigates 6-DOF joint attitude–trajectory planning for low-detectability spacecraft proximity operations under multiple third-party observation constraints. The resulting nonconvex optimal control problem is solved using an SCvx framework with cSTC-based conditional low-detectability constraints.

The main contributions of this paper are as follows:

1. A 6-DOF coupled attitude–trajectory model is formulated for low-detectability proximity operations of a unidirectional-thrust servicing spacecraft under multiple third-party space-based observation constraints. The model jointly incorporates the forward-looking camera, rear propulsion aperture, direction-dependent solar-array geometric blocking, and body-fixed main thrust, such that spacecraft attitude simultaneously affects target imaging, the prescribed low-detectability geometry, and the translational-control direction.
2. A position-dependent attitude-assisted low-detectability mechanism is introduced by formulating the rear-propulsion-aperture and solar-array blocking requirements, activated inside third-party observation FOVs, as compound state-triggered constraints. This formulation allows the servicing spacecraft to exploit attitude freedom after entering an observation FOV to adjust the direction-dependent geometry, thereby replacing part of the positional detour otherwise required by pure FOV avoidance.

The remainder of this paper is organized as follows. Section 2 formulates the 6-DOF joint attitude–trajectory proximity optimal control problem. Section 3 presents the SCvx solution method. Section 4 discusses the numerical results. Section 5 concludes the paper.

2. Modeling of the Six-Degree-of-Freedom Low-Detectability Proximity Problem

2.1. Conceptual Configuration of a Low-Detectability Servicing Spacecraft with Unidirectional Thrust

As early as the 1960s, the persistent external tracking of U.S. reconnaissance satellites motivated research on low-RCS and signature-suppression technologies for spacecraft. The U.S. Misty program is one of the early on-orbit low-detectability satellite projects reported in open sources [22]. The Tianxun-1 (TX-1) microsatellite developed by Nanjing University of Aeronautics and Astronautics further incorporated low-RCS requirements into the overall structural design. It has a multifaceted low-observable shape and includes body-mounted solar-cell arrays to control whole-spacecraft scattering characteristics while meeting basic functional requirements [23]. Building on this work, Sun and Qin [8] further optimized the low-observable shape, proposed the highly rotationally symmetric Olive-B configuration, and verified its favorable low-RCS performance through numerical computation and microwave anechoic chamber tests. However, these studies mainly focused on low-observable configurations and their RCS characteristics and did not consider an orbital propulsion system or its coupling with the low-observable configuration for active proximity missions. Therefore, based on the Olive-B configuration and fan-shaped solar array design, this paper further introduces a fixed forward-looking optical camera and a rear-mounted main-propulsion module to construct a conceptual model of a maneuverable low-detectability servicing spacecraft shown in Figure 1. This configuration is used to study the 6-DOF joint attitude–trajectory proximity problem under multiple space-based observation constraints.

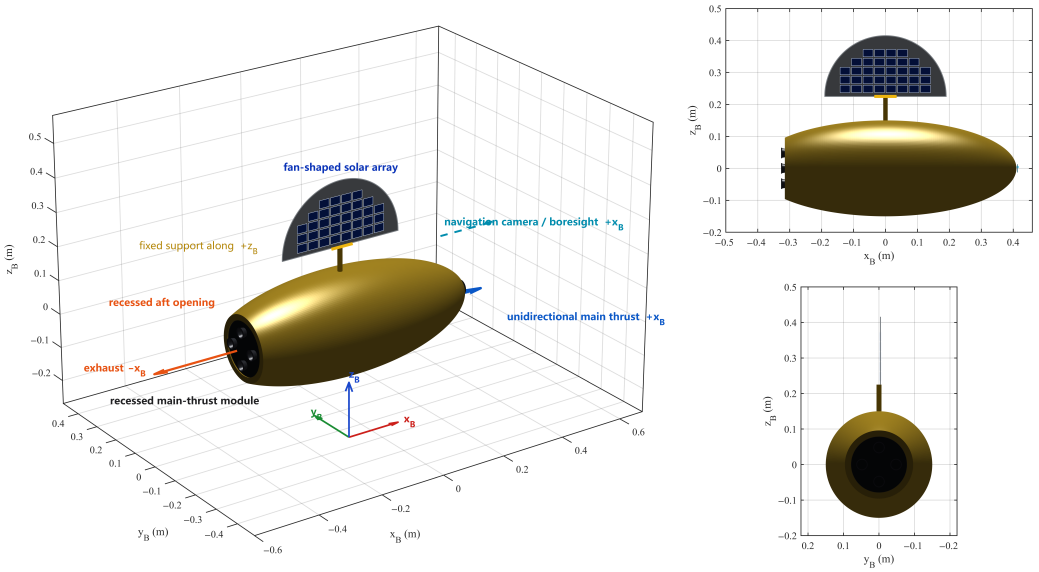


Figure 1. Olive-B-inspired conceptual configuration of a maneuverable low-detectability servicing spacecraft and definition of its body-fixed frame.

As shown in Figure 1, the optical navigation camera is fixed at the $+x_B$ end, with its optical axis aligned with the $+x_B$ direction. The main-propulsion system is located on the $-x_B$ side, and its resultant thrust acts along the $+x_B$ direction, while three-axis attitude control is provided by independent attitude actuators. The solar array is located on the $+z_B$ side, and its geometric relationship with the spacecraft body determines the geometric exposure of the solar array to a third-party observer. Thus, spacecraft attitude simultaneously affects the forward-looking camera pointing, the main-thrust direction, and the geometric blocking of the solar array by the spacecraft body, providing the physical basis for the subsequent 6-DOF joint attitude–trajectory planning.

2.2. Six-Degree-of-Freedom Coupled Attitude–Trajectory Dynamics

The target local-vertical/local-horizontal (LVLH) frame $\mathcal{F}_H$ is established with its origin at the center of mass of the target spacecraft, and the body-fixed frame of the servicing spacecraft is denoted by $\mathcal{F}_B$. The target spacecraft is assumed to operate in a near-circular orbit, and the relative distance between the servicing spacecraft and the target spacecraft is assumed to be much smaller than the orbital radius of the target spacecraft. During the short-duration near-field proximity operation considered in this paper, the orbital motion of the servicing spacecraft relative to the target spacecraft is described by the Clohessy–Wiltshire (CW) equations [24].

First, consider the relative orbital motion of the servicing spacecraft. Let the translational state be $\boldsymbol{x}_p = [\boldsymbol{r}^\top \ \boldsymbol{v}^\top]^\top \in \mathbb{R}^6$, where $\boldsymbol{r}, \boldsymbol{v} \in \mathbb{R}^3$ are the relative position and relative velocity expressed in the target LVLH frame $\mathcal{F}_H$, respectively. The relative translational dynamics are written as

$$\dot{\boldsymbol{x}}_p = A_p \boldsymbol{x}_p + B_p \frac{\boldsymbol{F}^H}{m} \tag{1}$$

where m is the mass of the servicing spacecraft and $\boldsymbol{F}^H \in \mathbb{R}^3$ is the control force expressed in the target LVLH frame, with

$$A_p = \begin{bmatrix} 0 & 0 & 0 & 1 & 0 & 0 \\ 0 & 0 & 0 & 0 & 1 & 0 \\ 0 & 0 & 0 & 0 & 0 & 1 \\ 3n^2 & 0 & 0 & 0 & 2n & 0 \\ 0 & 0 & 0 & -2n & 0 & 0 \\ 0 & 0 & -n^2 & 0 & 0 & 0 \end{bmatrix}, \qquad B_p = \begin{bmatrix} 0_{3\times 3} \\ I_3 \end{bmatrix}, \tag{2}$$

where n is the mean angular rate of the reference circular orbit of the target spacecraft.

Next, consider the attitude motion of the servicing spacecraft. Modified Rodrigues parameters (MRPs), $\boldsymbol{\sigma}_{BH} \in \mathbb{R}^3$, are used to describe the attitude of the body-fixed frame $\mathcal{F}_B$ of the servicing spacecraft relative to the target LVLH frame $\mathcal{F}_H$ [25]. Let the rotational state be $\boldsymbol{x}_r = [(\boldsymbol{\omega}_{BI}^B)^\top \ \boldsymbol{\sigma}_{BH}^\top]^\top \in \mathbb{R}^6$, where $\boldsymbol{\omega}_{BI}^B$ denotes the angular velocity of the servicing spacecraft body frame $\mathcal{F}_B$ relative to the inertial frame, expressed in the body frame. The direction-cosine matrix from $\mathcal{F}_H$ to $\mathcal{F}_B$ determined by $\boldsymbol{\sigma}_{BH}$ is denoted by $C_H^B(\boldsymbol{\sigma}_{BH})$ and is expressed as

$$C_H^B(\boldsymbol{\sigma}_{BH}) = I_3 - \frac{4(1 - \boldsymbol{\sigma}_{BH}^\top \boldsymbol{\sigma}_{BH})[\boldsymbol{\sigma}_{BH}]^\times - 8[\boldsymbol{\sigma}_{BH}]^\times [\boldsymbol{\sigma}_{BH}]^\times}{(1 + \boldsymbol{\sigma}_{BH}^\top \boldsymbol{\sigma}_{BH})^2}, \tag{3}$$

where $[\cdot]^\times$ denotes the skew-symmetric cross-product matrix corresponding to a three-dimensional vector.

The servicing spacecraft is treated as a rigid body, and its attitude control is provided by independent three-axis attitude actuators. The rigid-body rotational dynamics satisfy Euler's equation

$$\dot{\boldsymbol{\omega}}_{BI}^B = -J_B^{-1}[\boldsymbol{\omega}_{BI}^B]^\times J_B \boldsymbol{\omega}_{BI}^B + J_B^{-1}\boldsymbol{\tau}, \tag{4}$$

where J_B is the inertia matrix of the servicing spacecraft expressed in the body-fixed frame, and $\boldsymbol{\tau} \in \mathbb{R}^3$ is the attitude control torque.

Because the MRP $\boldsymbol{\sigma}_{BH}$ describes the attitude of the servicing spacecraft body frame relative to the target LVLH frame, its kinematics can be expressed in terms of the angular velocity relative to the LVLH frame. For a circular reference orbit, the angular velocity

of the target LVLH frame relative to the inertial frame is $\boldsymbol{\omega}_{HI}^{H} = [0\ 0\ n]^{\top}$. Therefore, the angular velocity of the servicing spacecraft body frame relative to the target LVLH frame is

$$\boldsymbol{\omega}_{BH}^{B} = \boldsymbol{\omega}_{BI}^{B} - C_{H}^{B}(\boldsymbol{\sigma}_{BH})\boldsymbol{\omega}_{HI}^{H}. \tag{5}$$

Define the MRP kinematic matrix as

$$B_{\sigma}(\boldsymbol{\sigma}_{BH}) = (1 - \boldsymbol{\sigma}_{BH}^{\top}\boldsymbol{\sigma}_{BH})I_3 + 2[\boldsymbol{\sigma}_{BH}]^{\times} + 2\boldsymbol{\sigma}_{BH}\boldsymbol{\sigma}_{BH}^{\top}. \tag{6}$$

The MRP attitude kinematics can then be written as

$$\dot{\boldsymbol{\sigma}}_{BH} = \frac{1}{4}B_{\sigma}(\boldsymbol{\sigma}_{BH})\boldsymbol{\omega}_{BH}^{B}. \tag{7}$$

Combining Equations (4) and (7), the attitude dynamics of the servicing spacecraft can be expressed as

$$\dot{\boldsymbol{x}}_r = \boldsymbol{f}_r(\boldsymbol{x}_r, \boldsymbol{\tau}). \tag{8}$$

The orbital and attitude motions described above are explicitly coupled through the direction of the unidirectional main thrust. According to the servicing spacecraft configuration shown in Figure 1, the main-propulsion system is located on the $-x_B$ side, and its resultant thrust is strictly aligned with the body-fixed $+x_B$ direction. Let $f \geq 0$ denote the thrust magnitude of the main-propulsion system. Then,

$$\boldsymbol{F}^{B} = f\boldsymbol{e}_1, \qquad \boldsymbol{F}^{H} = \left(C_{H}^{B}(\boldsymbol{\sigma}_{BH})\right)^{\top}\boldsymbol{e}_1 f, \qquad \boldsymbol{e}_1 = \begin{bmatrix} 1 & 0 & 0 \end{bmatrix}^{\top}. \tag{9}$$

Substituting the above control force into Equation (1) gives the attitude-dependent relative translational dynamics

$$\dot{\boldsymbol{x}}_p = A_p\boldsymbol{x}_p + B_p\frac{\left(C_{H}^{B}(\boldsymbol{\sigma}_{BH})\right)^{\top}\boldsymbol{e}_1 f}{m}, \tag{10}$$

which can be expressed as

$$\dot{\boldsymbol{x}}_p = \boldsymbol{f}_p(\boldsymbol{x}_p, \boldsymbol{x}_r, f). \tag{11}$$

As shown by Equation (10), the main-thrust direction is body-fixed, and the attitude $\boldsymbol{\sigma}_{BH}$ directly determines, through the direction-cosine matrix, the main-thrust direction in the target LVLH frame. Consequently, attitude not only affects the direction-dependent low-detectability geometry introduced below but also directly participates in translational control, thereby forming an explicit coupling mechanism in the 6-DOF attitude–trajectory dynamics.

Considering the main-thrust, attitude control torque, and angular rate limits, the associated magnitude constraints are

$$0 \leq f \leq f_{\max}, \qquad \|\boldsymbol{\tau}\|_2 \leq \tau_{\max}, \qquad \left\|\boldsymbol{\omega}_{BI}^{B}\right\|_2 \leq \omega_{\max}. \tag{12}$$

2.3. Direction-Dependent Low-Detectability Constraints

The servicing spacecraft considered in this paper is modeled using direction-dependent geometric conditions associated with favorable low-detectability observation directions. Changes in its attitude alter the geometric relationships between the rear propulsion aperture, solar array, spacecraft body, and the third-party observation line of sight. Based on the conceptual configuration shown in Figure 2, two mission-level geometric constraints are introduced: the rear-propulsion-aperture constraint and the solar-array geometric blocking constraint. These constraints serve as geometry-based proxies for favorable observation directions and describe only the relative geometry between the

servicing-spacecraft configuration and the observation line of sight; they do not directly model or predict the radar cross-section (RCS), optical brightness, infrared radiation, or detection probability.

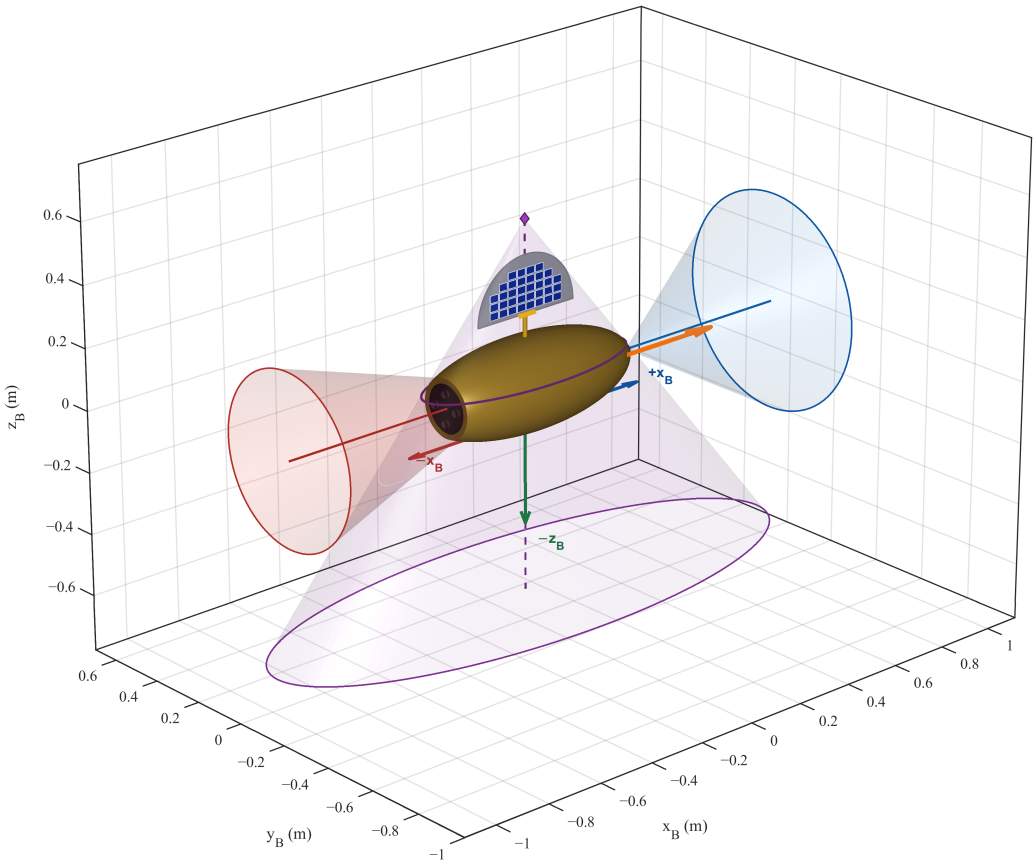


Figure 2. Direction-dependent low-detectability geometry in the servicing spacecraft body frame. The red cone denotes the rear-propulsion-aperture exclusion region along $-x_B$, the blue cone denotes the field of view of the forward-looking camera along $+x_B$, and the purple elliptical cone denotes observation directions for which the spacecraft body blocks the solar array.

2.3.1. Rear-Propulsion-Aperture Constraint

Let the position of the jth third-party observer be $\boldsymbol{r}_{G,j}$. The unit line of sight from the servicing spacecraft to this observer is expressed in the target LVLH frame $\mathcal{F}_H$ and the servicing spacecraft body frame $\mathcal{F}_B$, respectively, as

$$\boldsymbol{l}_{G,j}^{H} = \frac{\boldsymbol{r}_{G,j} - \boldsymbol{r}}{\left\|\boldsymbol{r}_{G,j} - \boldsymbol{r}\right\|_2}, \qquad \boldsymbol{l}_{G,j}^{B} = C_H^B(\boldsymbol{\sigma}_{BH})\boldsymbol{l}_{G,j}^{H}. \tag{13}$$

The main-propulsion module of the servicing spacecraft is located on the $-x_B$ side, and the axis of its rear propulsion aperture is $\boldsymbol{b}_a^B = -\boldsymbol{e}_1$. Let θ_a be the exclusion half-angle associated with the propulsion aperture. To prevent direct observation into the rear propulsion aperture, the constraint is expressed as

$$g_{a,j}(\boldsymbol{r}, \boldsymbol{\sigma}_{BH}) = (\boldsymbol{b}_a^B)^{\top} \boldsymbol{l}_{G,j}^{B} - \cos\theta_a \leq 0. \tag{14}$$

2.3.2. Solar-Array Geometric Blocking Constraint

The spacecraft body is approximated as an ellipsoid of revolution about the x_B axis. Because the solar array is fixed in its deployed configuration on the $+z_B$ side, the set of third-party observation directions for which the spacecraft body blocks the solar array is

approximated by an equivalent elliptical cone extending along the $-z_B$ direction, as shown in Figure 3.

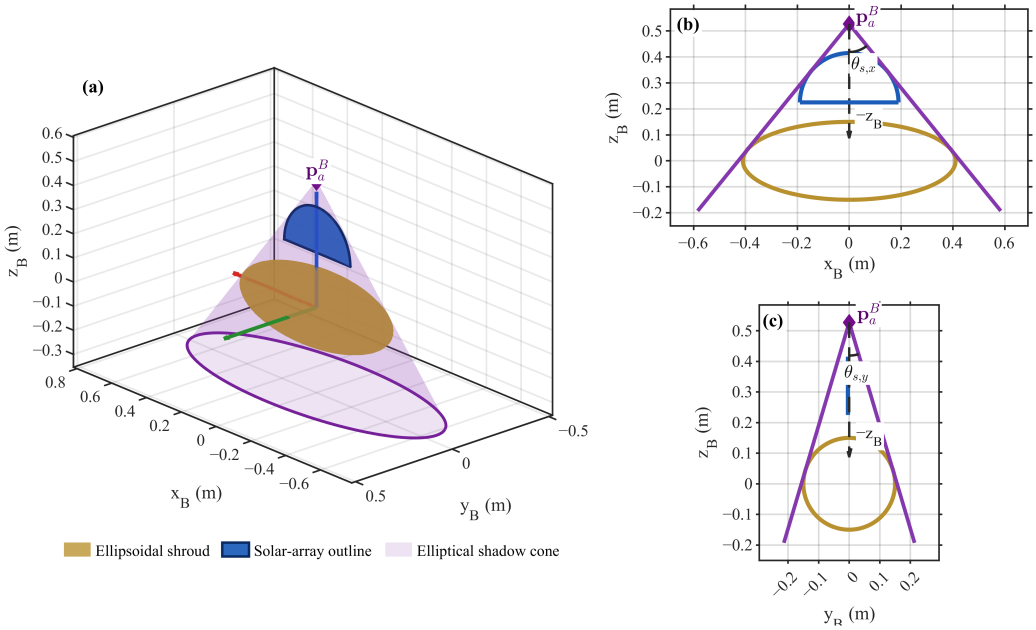


Figure 3. Construction of the equivalent elliptical cone: (**a**) three-dimensional equivalent elliptical cone; (**b**) tangency relation in the x_B–z_B principal section; and (**c**) tangency relation in the y_B–z_B principal section.

Let the position of the apex of this equivalent elliptical cone in the body frame be $\boldsymbol{p}_a^B$. The position of the jth third-party observer relative to the apex of the elliptical cone, expressed in the servicing spacecraft body frame, is

$$\boldsymbol{q}_j^B = C_H^B(\boldsymbol{\sigma}_{BH})(\boldsymbol{r}_{G,j} - \boldsymbol{r}) - \boldsymbol{p}_a^B. \tag{15}$$

Let the half-angles of this equivalent elliptical cone in the x_B–z_B and y_B–z_B principal sections be $\theta_{s,x}$ and $\theta_{s,y}$, respectively. The observation angular region satisfying the solar-array blocking condition can then be expressed as

$$g_{s,j}(\boldsymbol{r}, \boldsymbol{\sigma}_{BH}) = \left\| \begin{bmatrix} q_{j,x}^B / \tan\theta_{s,x} \\ q_{j,y}^B / \tan\theta_{s,y} \end{bmatrix} \right\|_2 + q_{j,z}^B \leq 0. \tag{16}$$

Equation (16) defines an elliptical-cone constraint that extends along the $-z_B$ direction with apex $\boldsymbol{p}_a^B$. The apex position $\boldsymbol{p}_a^B$ and the two half-angles in the principal sections $\theta_{s,x}$ and $\theta_{s,y}$ are predetermined from the idealized geometric relationship between the spacecraft body and the fixed deployed solar array. When Equation (16) is satisfied, the third-party observation direction lies within the equivalent elliptical cone so that the spacecraft body geometrically blocks the solar array. The equivalent cone is intended as a low-dimensional planning surrogate for the conceptual configuration rather than a high-fidelity visibility or signature model; for a detailed spacecraft design, its parameters may instead be obtained or replaced using CAD-based visibility analysis or direction-dependent signature data.

2.4. Mission and Observation Geometry Constraints

The servicing spacecraft is required to approach a prescribed inspection point $\boldsymbol{r}_f$ relative to the target spacecraft from a given initial state within a fixed mission duration t_f. Multiple third-party observing spacecraft with conical fields of view are present in the mission region. The overall mission geometry is shown in Figure 4.

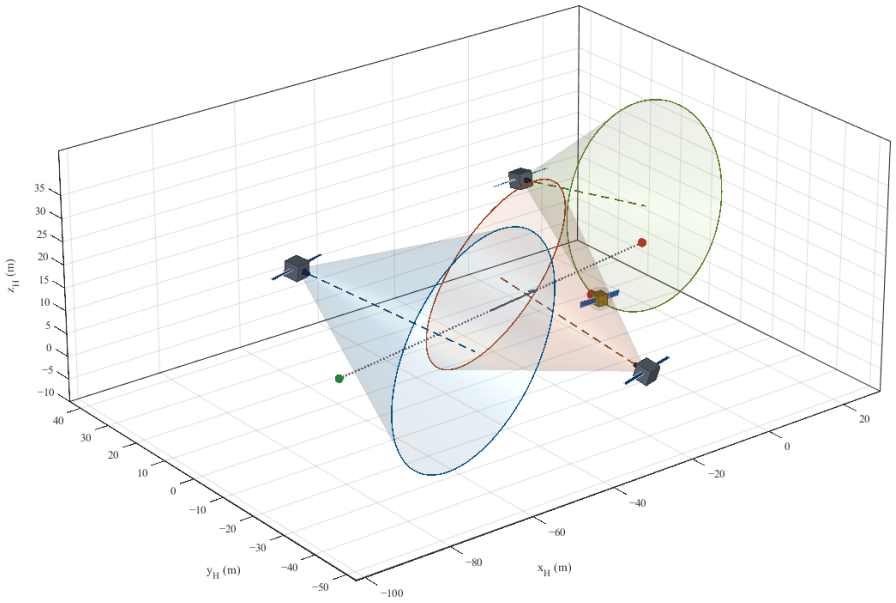


Figure 4. Low-detectability servicing spacecraft proximity scenario under multiple third-party observation constraints.

The initial and terminal boundary conditions are written as

$$\begin{cases} \boldsymbol{x}_p(0) = \boldsymbol{x}_{p,0}, & \boldsymbol{x}_r(0) = \boldsymbol{x}_{r,0}, \\ \boldsymbol{x}_p(t_f) = [\boldsymbol{r}_f^\top \ \mathbf{0}^\top]^\top, & \boldsymbol{\omega}_{BH}^B(t_f) = \mathbf{0}. \end{cases} \tag{17}$$

Here, $\boldsymbol{\omega}_{BH}^B$ is defined by Equation (5). The terminal attitude $\boldsymbol{\sigma}_{BH}(t_f)$ is not prescribed, allowing the servicing spacecraft to retain attitude-adjustment freedom while satisfying the requirements for forward imaging and direction-dependent low detectability. The specific mission duration, initial and terminal states, and dynamic parameters are given together in the numerical-simulation section.

To prevent collision between the servicing and target spacecraft, a spherical safety envelope of radius r_{koz} is used to describe the target keep-out zone (KOZ), requiring

$$g_{\text{koz}}(\boldsymbol{r}) = \frac{r_{\text{koz}}^2 - \boldsymbol{r}^\top \boldsymbol{r}}{r_{\text{koz}}^2} \leq 0. \tag{18}$$

The unit line of sight from the servicing spacecraft to the target spacecraft is defined as

$$\boldsymbol{l}_T^H = -\frac{\boldsymbol{r}}{\|\boldsymbol{r}\|_2}.$$

Because the optical navigation camera is fixed at the $+x_B$ end, the direction of its optical axis in the target LVLH frame is $\left(C_H^B(\boldsymbol{\sigma}_{BH})\right)^\top \boldsymbol{e}_1$. Let θ_{cam} denote the camera FOV half-angle. The target-imaging constraint is then written as

$$g_{\text{cam}}(\boldsymbol{r}, \boldsymbol{\sigma}_{BH}) = \cos\theta_{\text{cam}} - \boldsymbol{e}_1^\top C_H^B(\boldsymbol{\sigma}_{BH}) \boldsymbol{l}_T^H \leq 0. \tag{19}$$

Equation (19) constrains the body-fixed $+x_B$ axis to remain within θ_{cam} of the target line of sight while preserving roll freedom about that line of sight. This roll freedom enables attitude changes to adjust the direction-dependent low-detectability geometry of the servicing spacecraft relative to third-party observing spacecraft.

This paper focuses on close-range proximity planning with prescribed observation geometry. Over a single short-duration mission interval, the positions and observation

axes of the third-party observing spacecraft are treated as known parameters. There are N_G third-party observing spacecraft in the mission region. For the jth observing spacecraft, its position in $\mathcal{F}_H$ is denoted by $\boldsymbol{r}_{G,j}$, the unit vector along the center axis of its field of view by $\boldsymbol{d}_j^H$, and its half-field-of-view angle by $\theta_{G,j}$. The relative-position vector from the jth observing spacecraft to the servicing spacecraft is defined as

$$\boldsymbol{p}_j = \boldsymbol{r} - \boldsymbol{r}_{G,j}. \tag{20}$$

Accordingly, the field-of-view trigger function associated with the jth third-party observing spacecraft is defined as

$$g_{G,j}(\boldsymbol{r}) = \frac{(\boldsymbol{d}_j^H)^\top \boldsymbol{p}_j}{\|\boldsymbol{p}_j\|_2} - \cos\theta_{G,j}. \tag{21}$$

Therefore,

$$g_{G,j}(\boldsymbol{r}) \geq 0 \quad \Longleftrightarrow \quad \boldsymbol{r} \text{ is inside the } j\text{th observer FOV}. \tag{22}$$

The FOVs of the third-party observing spacecraft and the direction-dependent low-detectability geometry established in Section 2.3 correspond to constraints at two distinct levels. The former describes whether the servicing spacecraft lies within the observation range of a given third-party observing spacecraft, whereas the latter describes the favorable low-detectability geometric relationship that the servicing spacecraft configuration should satisfy for that third-party observation direction. Therefore, the rear-propulsion-aperture constraint and the solar-array blocking constraint are enforced only when the corresponding third-party FOV condition is triggered.

The corresponding mission-level conditional low-detectability requirement can be expressed as

$$g_{G,j}(\boldsymbol{r}) \geq 0 \quad \Longrightarrow \quad \left[g_{a,j}(\boldsymbol{r}, \boldsymbol{\sigma}_{BH}) \leq 0 \ \wedge \ g_{s,j}(\boldsymbol{r}, \boldsymbol{\sigma}_{BH}) \leq 0\right], \qquad j = 1, \ldots, N_G. \tag{23}$$

Equation (23) consists of one field-of-view trigger condition and two low-detectability constraint conditions that become active simultaneously and can be represented as a compound state-triggered constraint (cSTC). This expression describes the state-dependent conditional constraint in the original mission; its continuous representation and local convexification within the successive convexification framework are presented in Section 3.

2.5. Optimal Control Problem

For a fixed mission duration t_f, the objective function is defined as

$$J_{\text{ctrl}} = \int_0^{t_f} \left[w_f f(t) + w_\tau \|\boldsymbol{\tau}(t)\|_2\right] \mathrm{d}t, \tag{24}$$

Here, w_f and w_τ are the weights for translational propulsion and attitude control, respectively. The tradeoff between translational maneuvering and attitude adjustment is jointly determined by the coupled attitude–trajectory dynamics, the mission constraints, and Equation (24).

Combining the above dynamics, boundary conditions, mission constraints, and direction-dependent low-detectability constraints, the continuous-time six-degree-of-freedom joint attitude–trajectory optimal control problem $\mathcal{P}_0$ is written as

$$\mathcal{P}_0: \quad \min_{f(\cdot),\boldsymbol{\tau}(\cdot)} \quad J_{\text{ctrl}}, \tag{25a}$$

$$\text{s.t.} \quad \dot{\boldsymbol{x}}_r = \boldsymbol{f}_r(\boldsymbol{x}_r, \boldsymbol{\tau}), \tag{25b}$$

$$\dot{\boldsymbol{x}}_p = \boldsymbol{f}_p(\boldsymbol{x}_p, \boldsymbol{x}_r, f), \tag{25c}$$

$$\boldsymbol{x}_p(0) = \boldsymbol{x}_{p,0}, \qquad \boldsymbol{x}_r(0) = \boldsymbol{x}_{r,0}, \tag{25d}$$

$$\boldsymbol{x}_p(t_f) = [\boldsymbol{r}_f^\top \ \mathbf{0}^\top]^\top, \qquad \boldsymbol{\omega}_{BH}^B(t_f) = \mathbf{0}, \tag{25e}$$

$$g_{\text{koz}}(\boldsymbol{r}) \le 0, \tag{25f}$$

$$g_{\text{cam}}(\boldsymbol{r}, \boldsymbol{\sigma}_{BH}) \le 0, \tag{25g}$$

$$g_{G,j}(\boldsymbol{r}) \ge 0 \Longrightarrow \left[g_{a,j}(\boldsymbol{r}, \boldsymbol{\sigma}_{BH}) \le 0 \wedge g_{s,j}(\boldsymbol{r}, \boldsymbol{\sigma}_{BH}) \le 0\right], \qquad j = 1, \ldots, N_G, \tag{25h}$$

$$0 \le f \le f_{\max}, \qquad \|\boldsymbol{\tau}\|_2 \le \tau_{\max}, \tag{25i}$$

$$\|\boldsymbol{\omega}_{BI}^B\|_2 \le \omega_{\max}, \tag{25j}$$

The terminal attitude $\boldsymbol{\sigma}_{BH}(t_f)$ is not prescribed. Problem (25) includes nonlinear MRP attitude kinematics, attitude-dependent unidirectional thrust, the target keep-out-zone constraint, the camera FOV constraint, and direction-dependent low-detectability geometric constraints; it is therefore a nonconvex 6-DOF optimal control problem.

3. Successive Convexification Solution Framework

3.1. Model Linearization and Discretization

To solve the 6-DOF low-detectability proximity optimal control problem established in Section 2 using convex optimization, the nonlinear coupled attitude–trajectory dynamics are locally linearized about the current reference trajectory and then discretized into a finite-dimensional piecewise-affine system.

3.1.1. Linearization of the Six-Degree-of-Freedom Dynamics

Define the complete state and control vectors of the servicing spacecraft as

$$\boldsymbol{x} = \begin{bmatrix} \boldsymbol{x}_p^\top & \boldsymbol{x}_r^\top \end{bmatrix}^\top = \begin{bmatrix} \boldsymbol{r}^\top & \boldsymbol{v}^\top & (\boldsymbol{\omega}_{BI}^B)^\top & \boldsymbol{\sigma}_{BH}^\top \end{bmatrix}^\top \in \mathbb{R}^{12}, \qquad \boldsymbol{u} = \begin{bmatrix} f & \boldsymbol{\tau}^\top \end{bmatrix}^\top \in \mathbb{R}^4. \tag{26}$$

Combining Equations (8) and (11), the complete 6-DOF coupled attitude–trajectory dynamics can be expressed as

$$\dot{\boldsymbol{x}} = \boldsymbol{f}_x(\boldsymbol{x}, \boldsymbol{u}) = \begin{bmatrix} \boldsymbol{f}_p(\boldsymbol{x}_p, \boldsymbol{x}_r, f) \\ \boldsymbol{f}_r(\boldsymbol{x}_r, \boldsymbol{\tau}) \end{bmatrix}. \tag{27}$$

At the ith successive convexification iteration, a first-order Taylor expansion of $\boldsymbol{f}_x(\boldsymbol{x}, \boldsymbol{u})$ about the reference state and control trajectories $\bar{\boldsymbol{x}}^i(t)$ and $\bar{\boldsymbol{u}}^i(t)$ gives

$$\boldsymbol{f}_x(\boldsymbol{x}, \boldsymbol{u}) \approx \boldsymbol{f}_x(\bar{\boldsymbol{x}}^i, \bar{\boldsymbol{u}}^i) + \Lambda^i(t)(\boldsymbol{x} - \bar{\boldsymbol{x}}^i) + G^i(t)(\boldsymbol{u} - \bar{\boldsymbol{u}}^i), \tag{28}$$

where

$$\Lambda^i(t) = \left.\frac{\partial \boldsymbol{f}_x}{\partial \boldsymbol{x}}\right|_{\bar{\boldsymbol{x}}^i, \bar{\boldsymbol{u}}^i}, \qquad G^i(t) = \left.\frac{\partial \boldsymbol{f}_x}{\partial \boldsymbol{u}}\right|_{\bar{\boldsymbol{x}}^i, \bar{\boldsymbol{u}}^i} \tag{29}$$

are the Jacobian matrices of the complete 6-DOF dynamics with respect to the state and control, respectively.

Using $\boldsymbol{x} = [\boldsymbol{x}_p^\top \ \boldsymbol{x}_r^\top]^\top$ and $\boldsymbol{u} = [f \ \boldsymbol{\tau}^\top]^\top$ from Equation (26), the two Jacobian matrices can be written as

$$\Lambda^i = \begin{bmatrix} A_p & \Lambda_{pr}^i \\ 0_{6\times 6} & \Lambda_r^i \end{bmatrix}, \qquad G^i = \begin{bmatrix} G_{pf}^i & 0_{6\times 3} \\ 0_{6\times 1} & G_{r\tau} \end{bmatrix}. \tag{30}$$

Here, A_p is the CW system matrix defined in Equation (2). Because the translational dynamics in Equation (10) do not explicitly depend on the angular velocity $\boldsymbol{\omega}_{BI}^{B}$, but change the unidirectional main-thrust direction only through the attitude $\boldsymbol{\sigma}_{BH}$, it follows that $\Lambda_{pr}^{i} = [\, 0_{6\times 3} \;\; \Lambda_{p\sigma}^{i} \,]$, where

$$\Lambda_{p\sigma}^{i} = B_p \frac{\bar{f}^{i}}{m} \left. \frac{\partial \left[\left(C_H^B(\boldsymbol{\sigma}_{BH}) \right)^{\top} \boldsymbol{e}_1 \right]}{\partial \boldsymbol{\sigma}_{BH}} \right|_{\bar{\boldsymbol{\sigma}}_{BH}^{i}}. \tag{31}$$

This term describes the local first-order effect of changes in the main-thrust direction caused by attitude perturbations on the translational-state derivative and is the principal term coupling the attitude and trajectory dynamics under unidirectional thrust conditions.

The Jacobian of the translational dynamics with respect to thrust magnitude is

$$G_{pf}^{i} = B_p \frac{\left(C_H^B(\bar{\boldsymbol{\sigma}}_{BH}^{i}) \right)^{\top} \boldsymbol{e}_1}{m}, \tag{32}$$

whereas $G_{r\tau} = \begin{bmatrix} J_B^{-1} \\ 0_{3\times 3} \end{bmatrix}$.

For the rotational-state Jacobian in Equation (30), Equation (4) shows that the angular-velocity dynamics explicitly depend only on $\boldsymbol{\omega}_{BI}^{B}$ and the control torque $\boldsymbol{\tau}$ and not directly on the attitude parameter $\boldsymbol{\sigma}_{BH}$; by contrast, the MRP kinematics in Equation (7) depend on both $\boldsymbol{\omega}_{BI}^{B}$ and $\boldsymbol{\sigma}_{BH}$. Therefore, with the state ordering $\boldsymbol{x}_r = [(\boldsymbol{\omega}_{BI}^{B})^{\top} \; \boldsymbol{\sigma}_{BH}^{\top}]^{\top}$, one obtains

$$\Lambda_{r}^{i} = \begin{bmatrix} \Lambda_{\omega\omega}^{i} & 0_{3\times 3} \\ \Lambda_{\sigma\omega}^{i} & \Lambda_{\sigma\sigma}^{i} \end{bmatrix}, \tag{33}$$

where differentiating Equation (4) with respect to $\boldsymbol{\omega}_{BI}^{B}$ gives

$$\Lambda_{\omega\omega}^{i} = J_B^{-1} \Big([J_B \bar{\boldsymbol{\omega}}_{BI}^{B,i}]^{\times} - [\bar{\boldsymbol{\omega}}_{BI}^{B,i}]^{\times} J_B \Big). \tag{34}$$

Differentiating Equation (7) with respect to $\boldsymbol{\omega}_{BI}^{B}$ and using Equation (5) yields

$$\Lambda_{\sigma\omega}^{i} = \frac{1}{4} B_{\sigma}(\bar{\boldsymbol{\sigma}}_{BH}^{i}). \tag{35}$$

Because both the kinematic matrix $B_{\sigma}(\boldsymbol{\sigma}_{BH})$ in Equation (7) and the relative angular velocity $\boldsymbol{\omega}_{BH}^{B}$ in Equation (5) vary with the attitude $\boldsymbol{\sigma}_{BH}$, the qth column of the Jacobian of the MRP kinematics with respect to the attitude parameter is

$$\left[\Lambda_{\sigma\sigma}^{i} \right]_{:,q} = \frac{1}{4} \left[\left. \frac{\partial B_{\sigma}}{\partial \sigma_q} \right|_{\bar{\boldsymbol{\sigma}}_{BH}^{i}} \bar{\boldsymbol{\omega}}_{BH}^{B,i} - B_{\sigma}(\bar{\boldsymbol{\sigma}}_{BH}^{i}) \left. \frac{\partial C_H^B}{\partial \sigma_q} \right|_{\bar{\boldsymbol{\sigma}}_{BH}^{i}} \boldsymbol{\omega}_{HI}^{H} \right], \quad q = 1,2,3, \tag{36}$$

where $\bar{\boldsymbol{\omega}}_{BH}^{B,i} = \bar{\boldsymbol{\omega}}_{BI}^{B,i} - C_H^B(\bar{\boldsymbol{\sigma}}_{BH}^{i}) \boldsymbol{\omega}_{HI}^{H}$.

3.1.2. Discretization of the System Dynamics

To construct a finite-dimensional convex subproblem, the first-order linearized model in Equation (28) is written in the continuous-time linear time-varying affine form

$$\dot{\boldsymbol{x}} = \Lambda^{i}(t) \boldsymbol{x} + G^{i}(t) \boldsymbol{u} + \boldsymbol{c}^{i}(t), \tag{37}$$

where

$$\boldsymbol{c}^{i}(t) = \boldsymbol{f}_x(\bar{\boldsymbol{x}}^{i}(t), \bar{\boldsymbol{u}}^{i}(t)) - \Lambda^{i}(t) \bar{\boldsymbol{x}}^{i}(t) - G^{i}(t) \bar{\boldsymbol{u}}^{i}(t). \tag{38}$$

The fixed mission interval $[0, t_f]$ is discretized into N state nodes and $N-1$ control intervals:

$$0 = t_0 < t_1 < \cdots < t_{N-1} = t_f, \qquad \Delta t_k = t_{k+1} - t_k, \quad k = 0, \ldots, N-2. \tag{39}$$

A zero-order hold (ZOH) is applied over each control interval, i.e.,

$$\boldsymbol{u}(t) = \boldsymbol{u}_k, \qquad t \in [t_k, t_{k+1}), \quad k = 0, \ldots, N-2. \tag{40}$$

Let $\Phi^i(t, \tau)$ denote the state-transition matrix corresponding to the homogeneous linear time-varying system

$$\dot{\boldsymbol{z}} = \Lambda^i(t)\boldsymbol{z} \tag{41}$$

and let it satisfy $\Phi^i(\tau, \tau) = I_{12}$. The discrete system matrices associated with the kth control interval are then

$$\begin{aligned} A_k^i &= \Phi^i(t_{k+1}, t_k), \\ B_k^i &= \int_{t_k}^{t_{k+1}} \Phi^i(t_{k+1}, \tau) G^i(\tau)\, \mathrm{d}\tau, \\ \boldsymbol{c}_k^i &= \int_{t_k}^{t_{k+1}} \Phi^i(t_{k+1}, \tau) \boldsymbol{c}^i(\tau)\, \mathrm{d}\tau. \end{aligned} \tag{42}$$

The state-transition matrix and integral terms above are evaluated by numerical integration along the current reference trajectory at each successive convexification iteration.

Consequently, the continuous-time linear time-varying affine system can be discretized as

$$\boldsymbol{x}_{k+1} = A_k^i \boldsymbol{x}_k + B_k^i \boldsymbol{u}_k + \boldsymbol{c}_k^i, \qquad k = 0, \ldots, N-2. \tag{43}$$

Here, A_k^i, B_k^i, and $\boldsymbol{c}_k^i$ are the discrete state-transition matrix, control matrix, and constant term, respectively, associated with the kth control interval. Thus, at each successive convexification iteration, the original nonlinear 6-DOF coupled attitude–trajectory dynamics are locally approximated by a set of piecewise-affine discrete dynamic constraints.

Because the initial reference trajectory and the locally linearized models generated during the iterations may be dynamically infeasible, a virtual control $\boldsymbol{\nu}_k \in \mathbb{R}^{12}$ is introduced into the discrete dynamics. The dynamic constraint in the convex subproblem is therefore written as

$$\boldsymbol{x}_{k+1} = A_k^i \boldsymbol{x}_k + B_k^i \boldsymbol{u}_k + \boldsymbol{c}_k^i + \boldsymbol{\nu}_k, \qquad k = 0, \ldots, N-2. \tag{44}$$

The virtual control $\boldsymbol{\nu}_k$ prevents infeasibility of the convex subproblem caused by dynamic infeasibility of the initial reference trajectory or by local linearization error. It is heavily penalized in the objective function to drive it toward zero and does not correspond to any physical actuator.

3.2. Convexification of Path Constraints

The target keep-out-zone constraint, forward-camera field-of-view constraint, and conditional low-detectability constraints established in Section 2 all contain nonlinear state relationships and cannot be imposed directly as constraints in a convex subproblem. The thrust, control-torque, and angular-velocity magnitude constraints in Equation (12) are convex and can be retained directly at every successive convexification iteration; the remaining nonlinear path constraints are locally convexified to first order about the current reference trajectory.

3.2.1. First-Order Convexification of General Path Constraints

General nonlinear state constraints that do not involve conditional triggering are denoted uniformly by $g_l(\boldsymbol{x}_k) \leq 0$. At the ith successive convexification iteration, with the reference state $\bar{\boldsymbol{x}}_k^i$ as the linearization point, the local first-order convexification is written as

$$g_l(\bar{\boldsymbol{x}}_k^i) + \left[\nabla_{\boldsymbol{x}} g_l(\bar{\boldsymbol{x}}_k^i)\right]^\top \left(\boldsymbol{x}_k - \bar{\boldsymbol{x}}_k^i\right) \leq s_{l,k}, \qquad s_{l,k} \geq 0, \tag{45}$$

Here, $s_{l,k}$ is a nonnegative slack variable that prevents the convex subproblem from becoming infeasible when the reference trajectory violates nonlinear path constraints during early iterations; it is penalized in the objective function to drive it toward zero.

The target keep-out-zone constraint in Equation (18) depends only on the relative position $\boldsymbol{r}$. A first-order expansion about the reference position $\bar{\boldsymbol{r}}_k^i$ gives

$$\frac{r_{\text{koz}}^2 + \|\bar{\boldsymbol{r}}_k^i\|_2^2 - 2(\bar{\boldsymbol{r}}_k^i)^\top \boldsymbol{r}_k}{r_{\text{koz}}^2} \leq s_{\text{koz},k}. \tag{46}$$

The forward-camera field-of-view constraint in Equation (19) depends on both the relative position $\boldsymbol{r}$ and the attitude $\boldsymbol{\sigma}_{BH}$. Linearizing about the reference state $(\bar{\boldsymbol{r}}_k^i, \bar{\boldsymbol{\sigma}}_{BH,k}^i)$ gives

$$g_{\text{cam}}(\bar{\boldsymbol{r}}_k^i, \bar{\boldsymbol{\sigma}}_{BH,k}^i) + [\nabla_{\boldsymbol{r}} g_{\text{cam}}]_{i,k}^\top (\boldsymbol{r}_k - \bar{\boldsymbol{r}}_k^i) + [\nabla_{\boldsymbol{\sigma}} g_{\text{cam}}]_{i,k}^\top (\boldsymbol{\sigma}_{BH,k} - \bar{\boldsymbol{\sigma}}_{BH,k}^i) \leq s_{\text{cam},k}, \tag{47}$$

The corresponding gradients are evaluated at the reference state $(\bar{\boldsymbol{r}}_k^i, \bar{\boldsymbol{\sigma}}_{BH,k}^i)$. Because activation of the conditional low-detectability constraints in Equation (23) depends on the position of the servicing spacecraft relative to the third-party FOVs, their continuous representation and local convexification are presented in the next subsection.

In addition, the terminal relative-angular-velocity constraint $\boldsymbol{\omega}_{BH}^B(t_f) = \mathbf{0}$ also contains attitude-dependent nonlinearity. Define $\boldsymbol{h}_f(\boldsymbol{x}) = \boldsymbol{\omega}_{BI}^B - C_H^B(\boldsymbol{\sigma}_{BH})\boldsymbol{\omega}_{HI}^H$. Its first-order approximation about the reference terminal state at the ith iteration is

$$\boldsymbol{h}_f(\bar{\boldsymbol{x}}_{N-1}^i) + \left.\frac{\partial \boldsymbol{h}_f}{\partial \boldsymbol{x}}\right|_{\bar{\boldsymbol{x}}_{N-1}^i} (\boldsymbol{x}_{N-1} - \bar{\boldsymbol{x}}_{N-1}^i) = \mathbf{0}. \tag{48}$$

3.2.2. Convexification of the Compound State-Triggered Constraints

The conditional low-detectability constraints in Equation (23) contain discrete triggering logic determined by the position state of the servicing spacecraft and therefore cannot be embedded directly in a continuous optimization framework. Following the treatment of compound state-triggered constraints by Zhang et al. [21], the field-of-view trigger factor for the jth third-party observing spacecraft is defined as

$$\alpha_{G,j}(\boldsymbol{r}) = -\min\{-g_{G,j}(\boldsymbol{r}), 0\}, \tag{49}$$

Here, $g_{G,j}(\boldsymbol{r})$ is defined by Equation (21). It follows from Equation (49) that when the servicing spacecraft lies inside the jth observation field of view, i.e., $g_{G,j}(\boldsymbol{r}) > 0$, one has $\alpha_{G,j} = g_{G,j} > 0$; when the servicing spacecraft lies outside that field of view, i.e., $g_{G,j}(\boldsymbol{r}) < 0$, one has $\alpha_{G,j} = 0$.

Accordingly, the two low-detectability conditions in Equation (23) are constructed in the following form:

$$\begin{aligned} h_{a,j}(\boldsymbol{x}) &= \alpha_{G,j}(\boldsymbol{r}) g_{a,j}(\boldsymbol{r}, \boldsymbol{\sigma}_{BH}) \leq 0, \\ h_{s,j}(\boldsymbol{x}) &= \alpha_{G,j}(\boldsymbol{r}) g_{s,j}(\boldsymbol{r}, \boldsymbol{\sigma}_{BH}) \leq 0, \end{aligned} \tag{50}$$

Here, $\boldsymbol{x}$ is defined by Equation (26). When $g_{G,j} > 0$, because $\alpha_{G,j} > 0$, the two relations in Equation (50) are equivalent to $g_{a,j} \leq 0$ and $g_{s,j} \leq 0$, respectively. When $g_{G,j} < 0$, $\alpha_{G,j} = 0$, and the corresponding low-detectability constraints are inactive. Therefore, without introducing integer variables, Equation (50) provides a continuous-optimization representation of the original state-dependent conditional-triggering logic.

Despite this continuous reformulation, $h_{a,j}$ and $h_{s,j}$ still contain nonlinear coupling between the trigger function and the direction-dependent geometric constraints and therefore require a further local first-order approximation at each successive convexification iteration. For compactness, let $q \in \{a, s\}$ and denote both constraints uniformly by

$$h_{q,j}(\boldsymbol{x}) = \alpha_{G,j}(\boldsymbol{r}) g_{q,j}(\boldsymbol{r}, \sigma_{BH}). \tag{51}$$

At the kth discrete node of the ith iteration, its local first-order approximation, according to whether the reference state lies inside the corresponding FOV, is written as

$$\widehat{h}^{i}_{q,j,k}(\boldsymbol{x}_k) = \begin{cases} h_{q,j}(\bar{\boldsymbol{x}}^{i}_{k}) + \left[\nabla_{\boldsymbol{x}} h_{q,j}(\bar{\boldsymbol{x}}^{i}_{k})\right]^{\top} (\boldsymbol{x}_k - \bar{\boldsymbol{x}}^{i}_{k}), & g_{G,j}(\bar{\boldsymbol{r}}^{i}_{k}) > 0, \\ 0, & g_{G,j}(\bar{\boldsymbol{r}}^{i}_{k}) \leq 0, \end{cases} \qquad q \in \{a, s\}. \tag{52}$$

For a node whose reference state lies inside the observation field of view, $\alpha_{G,j} = g_{G,j}$. Therefore, by the product rule, the gradient required in Equation (52) is

$$\nabla_{\boldsymbol{x}} h_{q,j} = g_{q,j} \nabla_{\boldsymbol{x}} g_{G,j} + g_{G,j} \nabla_{\boldsymbol{x}} g_{q,j}, \qquad q \in \{a, s\}, \tag{53}$$

All functions and gradients in this expression are evaluated at the current reference state $\bar{\boldsymbol{x}}^{i}_{k}$. Because $g_{G,j}$ depends only on the relative position $\boldsymbol{r}$, whereas $g_{a,j}$ and $g_{s,j}$ depend on both $\boldsymbol{r}$ and σ_{BH}, Equation (53) naturally retains the local coupling between the observation-field triggering state and the low-detectability geometry of the servicing spacecraft.

In the ith convex subproblem, the following constraints are imposed for every third-party observing spacecraft and discrete node:

$$\widehat{h}^{i}_{a,j,k}(\boldsymbol{x}_k) \leq s_{a,j,k}, \qquad \widehat{h}^{i}_{s,j,k}(\boldsymbol{x}_k) \leq s_{s,j,k}, \tag{54}$$

where $s_{a,j,k} \geq 0$ and $s_{s,j,k} \geq 0$.

It should be noted that at the observation-field boundary $g_{G,j}(\boldsymbol{r}) = 0$, the trigger factor in Equation (49) degenerates to zero, and the continuous cSTC undergoes a piecewise transition. Therefore, Equation (50) and its local approximation are used primarily to construct a continuous optimization model during successive convexification. The final feasibility of a candidate trajectory is still assessed a posteriori using the original closed-set observation FOV defined by Equation (21). At every node satisfying $g_{G,j}(\boldsymbol{r}_k) \geq 0$, the original rear-propulsion-aperture constraint $g_{a,j} \leq 0$ and solar-array blocking constraint $g_{s,j} \leq 0$, without multiplication by the trigger factor, are checked directly. This prevents trigger degeneration at the field-of-view boundary from concealing an actual constraint violation.

3.3. Convex Subproblem and Hard Trust Regions

Combining the dynamic discretization, convexification of general path constraints, and local convexification of the cSTCs described above, hard trust region constraints are imposed at the ith iteration on the deviations of each state and control block from the current reference trajectory, so as to limit the validity range of the local linear model:

$$\begin{cases} \|\boldsymbol{r}_k - \bar{\boldsymbol{r}}^{i}_{k}\|_2 \leq \delta^{i}_{r}, & \|\boldsymbol{v}_k - \bar{\boldsymbol{v}}^{i}_{k}\|_2 \leq \delta^{i}_{v}, \\ \|\boldsymbol{\omega}^{B}_{BI,k} - \bar{\boldsymbol{\omega}}^{B,i}_{BI,k}\|_2 \leq \delta^{i}_{\omega}, & \|\boldsymbol{\sigma}_{BH,k} - \bar{\boldsymbol{\sigma}}^{i}_{BH,k}\|_2 \leq \delta^{i}_{\sigma}. \end{cases} \tag{55}$$

$$|f_k - \bar{f}_k^i| \le \delta_f^i, \qquad \|\boldsymbol{\tau}_k - \bar{\boldsymbol{\tau}}_k^i\|_2 \le \delta_\tau^i. \tag{56}$$

Define the state and control trust region radius vectors, respectively, as $\boldsymbol{\delta}_x^i = \begin{bmatrix}\delta_r^i & \delta_v^i & \delta_\omega^i & \delta_\sigma^i\end{bmatrix}^\top$, $\boldsymbol{\delta}_u^i = \begin{bmatrix}\delta_f^i & \delta_\tau^i\end{bmatrix}^\top$.

Each trust region radius is set according to the scale of the corresponding physical quantity, and the radii are adjusted synchronously during the iterations according to the local-model agreement. Let $\boldsymbol{s}_k$ collect all nonnegative slack variables associated with the general path constraints and cSTCs at node k. The following second-order cone subproblem is then solved at the ith iteration:

$$\min_{\{\boldsymbol{x}_k,\boldsymbol{u}_k,\boldsymbol{\nu}_k,\boldsymbol{s}_k\}} \quad J_{\text{ctrl}}^d + \lambda_\nu \sum_{k=0}^{N-2} \|\boldsymbol{\nu}_k\|_1 + \lambda_s \sum_{k=0}^{N-1} \|\boldsymbol{s}_k\|_1, \tag{57a}$$

$$\text{s.t.} \quad \boldsymbol{x}_{k+1} = A_k^i \boldsymbol{x}_k + B_k^i \boldsymbol{u}_k + \boldsymbol{c}_k^i + \boldsymbol{\nu}_k, \qquad k = 0, \dots, N-2, \tag{57b}$$

$$g_l(\bar{\boldsymbol{x}}_k^i) + \left[\nabla_x g_l(\bar{\boldsymbol{x}}_k^i)\right]^\top (\boldsymbol{x}_k - \bar{\boldsymbol{x}}_k^i) \le s_{l,k}, \tag{57c}$$

$$\widehat{h}_{a,j,k}^i(\boldsymbol{x}_k) \le s_{a,j,k}, \qquad \widehat{h}_{s,j,k}^i(\boldsymbol{x}_k) \le s_{s,j,k}, \qquad j = 1, \dots, N_G, \tag{57d}$$

$$\boldsymbol{x}_0 = [\boldsymbol{x}_{p,0}^\top \, \boldsymbol{x}_{r,0}^\top]^\top, \qquad \boldsymbol{x}_{p,N-1} = [\boldsymbol{r}_f^\top \, \boldsymbol{0}^\top]^\top, \tag{57e}$$

$$\boldsymbol{h}_f(\bar{\boldsymbol{x}}_{N-1}^i) + \left.\frac{\partial \boldsymbol{h}_f}{\partial \boldsymbol{x}}\right|_{\bar{\boldsymbol{x}}_{N-1}^i} (\boldsymbol{x}_{N-1} - \bar{\boldsymbol{x}}_{N-1}^i) = \boldsymbol{0}, \tag{57f}$$

$$0 \le f_k \le f_{\max}, \qquad \|\boldsymbol{\tau}_k\|_2 \le \tau_{\max}, \qquad \|\boldsymbol{\omega}_{BI,k}^B\|_2 \le \omega_{\max}, \tag{57g}$$

$$\text{Equations (55) and (56)}, \qquad \boldsymbol{s}_k \succeq \boldsymbol{0}. \tag{57h}$$

Here, $J_{\text{ctrl}}^d = \sum_{k=0}^{N-2} \left(w_f f_k + w_\tau \|\boldsymbol{\tau}_k\|_2\right) \Delta t_k$ is the discrete form of Equation (24). The positive constants λ_ν and λ_s are the penalty weights associated with the virtual-control and path-slack variables, respectively. They are selected to be sufficiently larger than the physical control weights so that artificial feasibility restoration is strongly penalized relative to the nominal control objective. The same weighting parameters are used for all comparison cases.

3.4. SCvx Iteration

The optimal solution $\{\boldsymbol{x}_k^\star, \boldsymbol{u}_k^\star\}$ of the convex subproblem is taken as the current candidate trajectory. To assess the predictive consistency of the local convex model with the original nonlinear problem, define the nonlinear merit function

$$\mathcal{J}(\boldsymbol{X}, \boldsymbol{U}) = J_{\text{ctrl}}^d(\boldsymbol{U}) + \lambda_\nu V_{\text{dyn}}(\boldsymbol{X}, \boldsymbol{U}) + \lambda_s V_{\text{path}}(\boldsymbol{X}), \tag{58}$$

Here, $\boldsymbol{X}$ and $\boldsymbol{U}$ denote the discrete state and control sequences, respectively; V_{dyn} is the sum of the L_1 norms of the dynamic defects obtained by propagating the candidate nodal trajectory interval by interval using the original nonlinear dynamics, and V_{path} is the sum of the positive violations of the path constraints.

Correspondingly, denote the local merit function associated with the ith convex subproblem in Equation (57a) by $\mathcal{L}_i$, and denote its values at the zero step corresponding to the current reference trajectory and at the optimal candidate point of the convex subproblem by $\mathcal{L}_i^0$ and $\mathcal{L}_i^\star$, respectively. The actual reduction and reduction predicted by the local model are defined as

$$\Delta\mathcal{J}_i^{\text{act}} = \mathcal{J}(\bar{\boldsymbol{X}}^i, \bar{\boldsymbol{U}}^i) - \mathcal{J}(\boldsymbol{X}^\star, \boldsymbol{U}^\star), \qquad \Delta\mathcal{J}_i^{\text{pred}} = \mathcal{L}_i^0 - \mathcal{L}_i^\star. \tag{59}$$

When $\Delta\mathcal{J}_i^{\text{pred}} > 0$, define the reduction ratio $\rho_i = \Delta\mathcal{J}_i^{\text{act}} / \Delta\mathcal{J}_i^{\text{pred}}$, which measures the accuracy with which the local convex model predicts the change in the nonlinear merit

function. It is used to accept or reject the candidate trajectory and to adjust the trust region radii of the individual physical blocks.

For a sequence of iterates, let $\mathcal{J}^i = \mathcal{J}(\bar{\boldsymbol{X}}^i, \bar{\boldsymbol{U}}^i)$. The relative change in the merit function between two consecutive updates is defined as

$$\epsilon_J^i = \frac{\left|\mathcal{J}^{i+1} - \mathcal{J}^i\right|}{\max\{1, \left|\mathcal{J}^i\right|\}}. \tag{60}$$

When $\epsilon_J^i \le \epsilon_J$, the normal SCvx iteration-termination condition is considered satisfied. The detailed iterative procedure is given in Algorithm 1.

Algorithm 1 cSTC-based SCvx algorithm for the low-detectability proximity mission.

Input: $\{\bar{\boldsymbol{x}}_k^0, \bar{\boldsymbol{u}}_k^0\}$, (δ_x^0, δ_u^0), $\lambda_v, \lambda_s, \epsilon_J$
Output: $\{\boldsymbol{x}_k^\star, \boldsymbol{u}_k^\star\}$
$i \leftarrow 0$
while true do
  Solve the convex subproblem in (57). $\rightarrow \{\boldsymbol{x}_k^\star, \boldsymbol{u}_k^\star\}$
  $(\Delta\mathcal{J}_i^{\text{act}}, \Delta\mathcal{J}_i^{\text{pred}}) \leftarrow$ (59)
  if $\Delta\mathcal{J}_i^{\text{pred}} \le 0$ **then**
    $(\delta_x^i, \delta_u^i) \leftarrow 0.5(\delta_x^i, \delta_u^i)$
  else
    $\rho_i \leftarrow \Delta\mathcal{J}_i^{\text{act}} / \Delta\mathcal{J}_i^{\text{pred}}$
    if $\rho_i < 0$ **then**
      $(\delta_x^i, \delta_u^i) \leftarrow 0.5(\delta_x^i, \delta_u^i)$
    else
      $\{\bar{\boldsymbol{x}}_k^{i+1}, \bar{\boldsymbol{u}}_k^{i+1}\} \leftarrow \{\boldsymbol{x}_k^\star, \boldsymbol{u}_k^\star\}$
      $(\delta_x^{i+1}, \delta_u^{i+1}) \leftarrow \begin{cases} 0.5(\delta_x^i, \delta_u^i), & \rho_i < 0.25, \\ 2(\delta_x^i, \delta_u^i), & \rho_i \ge 0.7, \\ (\delta_x^i, \delta_u^i), & \text{otherwise.} \end{cases}$
      $\epsilon_J^i \leftarrow$ (60)
      if $\epsilon_J^i \le \epsilon_J$ **then**
        $\{\boldsymbol{x}_k^\star, \boldsymbol{u}_k^\star\} \leftarrow \{\bar{\boldsymbol{x}}_k^{i+1}, \bar{\boldsymbol{u}}_k^{i+1}\}$
        return $\{\boldsymbol{x}_k^\star, \boldsymbol{u}_k^\star\}$
      end if
      $i \leftarrow i + 1$
    end if
  end if
end while

4. Numerical Simulations

4.1. Simulation Parameters and Scenario Setup

To evaluate the proposed attitude-assisted scheme, a fixed terminal time, uniformly spaced state nodes, and piecewise-constant control are adopted. The servicing spacecraft approaches a prescribed terminal inspection position relative to the target spacecraft from a given initial state, while the terminal attitude is not prescribed. The path constraints are imposed at the discrete state nodes of the transcription, and the limitation associated with possible inter-sample constraint violations is discussed separately in the subsequent results. The principal physical and mission parameters are listed in Table 1.

Table 1. Principal physical and mission parameters.

Parameter	Value
Mission duration t_f	300 s
State nodes N	140
Initial relative position $\boldsymbol{r}_0$	$[-90, -32, 20]^\top$ m
Terminal inspection position $\boldsymbol{r}_f$	$[18, 8, 5]^\top$ m
Initial and terminal relative velocities $\boldsymbol{v}_0, \boldsymbol{v}_f$	$\mathbf{0}$
Servicing spacecraft mass m	61 kg
Inertia matrix J_B	$\mathrm{diag}(0.5490, 2.3253, 2.3253)$ kg m^2
Maximum main thrust $f_{\max}$	1 N
Maximum control torque $\tau_{\max}$	0.02 N m
Maximum angular velocity $\omega_{\max}$	1 rad/s
Target KOZ radius r_{koz}	2.5 m
Camera FOV half-angle θ_{cam}	30°
Third-party observer FOV half-angle $\theta_{G,j}$	30°
Rear-aperture half-angle θ_a	16.95°
Principal half-angles $\theta_{s,x}/\theta_{s,y}$	39.06°/16.54°

Note: The bold symbol $\mathbf{0}$ denotes a three-dimensional zero vector.

The two comparison schemes use identical initial trajectories, state and control bounds, discretization grids, objective functions, penalty weights, and SCvx trust region parameters. The initial position trajectory is obtained by linear interpolation between the initial and terminal positions, and the controls are initialized to zero. This initial guess may be dynamically infeasible, with the resulting infeasibility handled by the virtual control and trust region mechanisms in SCvx. Because SCvx solves the underlying nonconvex optimal-control problem locally, the resulting solution may depend on the initialization; a systematic multi-start robustness study is beyond the scope of the present work. The principal solver parameters are listed in Table 2.

Table 2. Principal numerical settings for SCvx.

Parameter	Value
Virtual control penalty weight λ_ν	3×10^5
Path slack penalty weight λ_s	1×10^6
Control weights (w_f, w_τ)	$(1, 0.05)$
Initial position trust region radius δ_r^0	6 m
Initial velocity trust region radius δ_v^0	0.5 m/s
Initial angular velocity trust region radius δ_ω^0	0.08 rad/s
Initial MRP trust region radius δ_σ^0	0.04
Initial main thrust trust region radius δ_f^0	0.25 N
Initial control torque trust region radius δ_τ^0	5×10^{-3} N m
Relative merit-function-change termination threshold ϵ_J	10^{-2}

The computations were performed on a desktop computer equipped with a 12th Gen Intel Core i5-12400 processor and 32 GB of RAM. The convex subproblems were modeled using CVX and solved with MOSEK.

Two mission formulations were compared with identical dynamics, boundary conditions, state and control bounds, discretization, objective weights, initialization, penalty weights, and SCvx settings. The attitude-assisted formulation allows the servicing spacecraft to enter the FOVs of the third-party observing spacecraft, while requiring the corresponding direction-dependent geometric constraints to be satisfied when an observation FOV is active. In contrast, the FOV-avoidance formulation requires the servicing spacecraft to remain outside all third-party FOVs throughout the mission. Therefore, the two

formulations have different feasible sets, and the comparison is intended to assess the effect of introducing attitude-assisted observation geometry rather than the performance of different numerical optimization algorithms. Both formulations were solved using the same SCvx framework.

4.2. Comparison of Simulation Results

Figure 5 shows the optimized trajectories of the attitude-assisted scheme and the FOV-avoidance scheme in the main case. The blue solid curve denotes the attitude-assisted scheme, and the orange dashed curve denotes the FOV-avoidance scheme; the short red and green axes indicate the body-fixed $+x_B$ direction and the $-z_B$ direction, respectively, at selected discrete nodes of the attitude-assisted solution. The attitude-assisted scheme passes through the three third-party observation regions approximately along the direct path between the initial and terminal positions, while the prescribed direction-dependent geometric constraints are satisfied at the FOV-active transcription nodes through attitude adjustment. Because entry into the observation fields of view is prohibited in the FOV-avoidance scheme, it must detour around the observation cones, resulting in an evident positional deviation during the middle part of the mission. The final path lengths of the two schemes are 116.16 m and 125.22 m, respectively. This result shows that using attitude freedom to adjust the solar-array blocking relationship can reduce the need for trajectory detours.

Figure 6 further presents a nodal a posteriori evaluation obtained by substituting the final candidate trajectories of the two schemes into the original nonlinear path constraints at the transcription nodes. In Figure 6a, $g_{G,j} \geq 0$ indicates that the servicing spacecraft is inside the field of view of the jth third-party observing spacecraft. In the attitude-assisted scheme, 35, 42, and 22 nodes lie within the three fields of view, respectively, for a total of 99 FOV-active nodes; the FOV-avoidance scheme has no FOV-active nodes. The tightest nodes for the first two observers lie near the FOV boundaries, indicating that the FOV-avoidance solution tends to form a tightly constrained detour trajectory along the boundaries of the observation cones.

Figure 6b shows that the camera FOV constraint is satisfied at all transcription nodes for both schemes. Although the FOV-avoidance scheme uses position freedom to avoid the third-party FOVs, it remains subject to the attitude constraint that the forward camera continuously point toward the target.

Figure 6c,d plot only the original directional constraints of the attitude-assisted scheme at FOV-active nodes. All activated nodes satisfy $g_{s,j} \leq 0$ and $g_{a,j} \leq 0$. Thus, although the servicing spacecraft enters the third-party FOVs multiple times, it satisfies the original rear-aperture and solar-array blocking conditions at every FOV-active node. $g_{s,j}$ approaches its constraint boundary at several FOV-active nodes, indicating that the solar-array blocking constraint is locally active in shaping the attitude solution.

Figure 7 shows the control and angular-velocity histories of the two schemes. Figure 7a shows the unidirectional main-thrust magnitude f. Because the FOV-avoidance scheme must detour substantially around the third-party observation cones, it requires greater control effort for translational acceleration, turning, and terminal deceleration. The total thrust impulse of the attitude-assisted scheme is $I_F^{\mathrm{att}} = 51.7662\,\mathrm{N\,s}$, whereas that of the FOV-avoidance scheme is $I_F^{\mathrm{pos}} = 94.7195\,\mathrm{N\,s}$, corresponding to a 45.35% reduction in the considered main scenario.

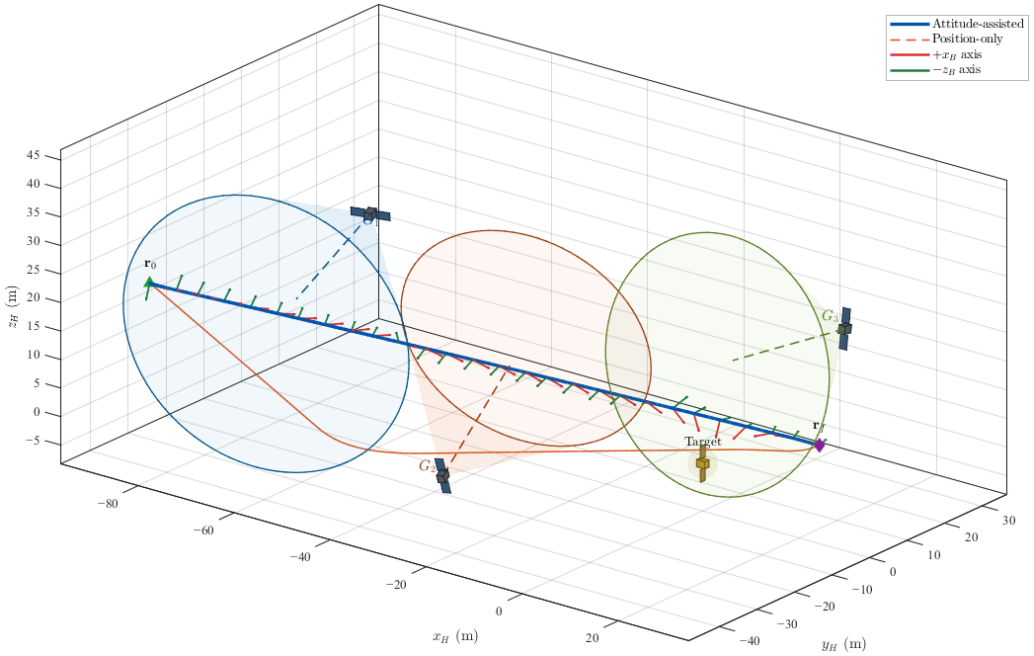


Figure 5. Comparison of the three-dimensional optimized trajectories of the attitude-assisted scheme and the FOV-avoidance scheme in the main case. The short red and green axes represent the body-fixed $+x_B$ direction and the $-z_B$ direction, respectively, at selected discrete nodes of the attitude-assisted solution.

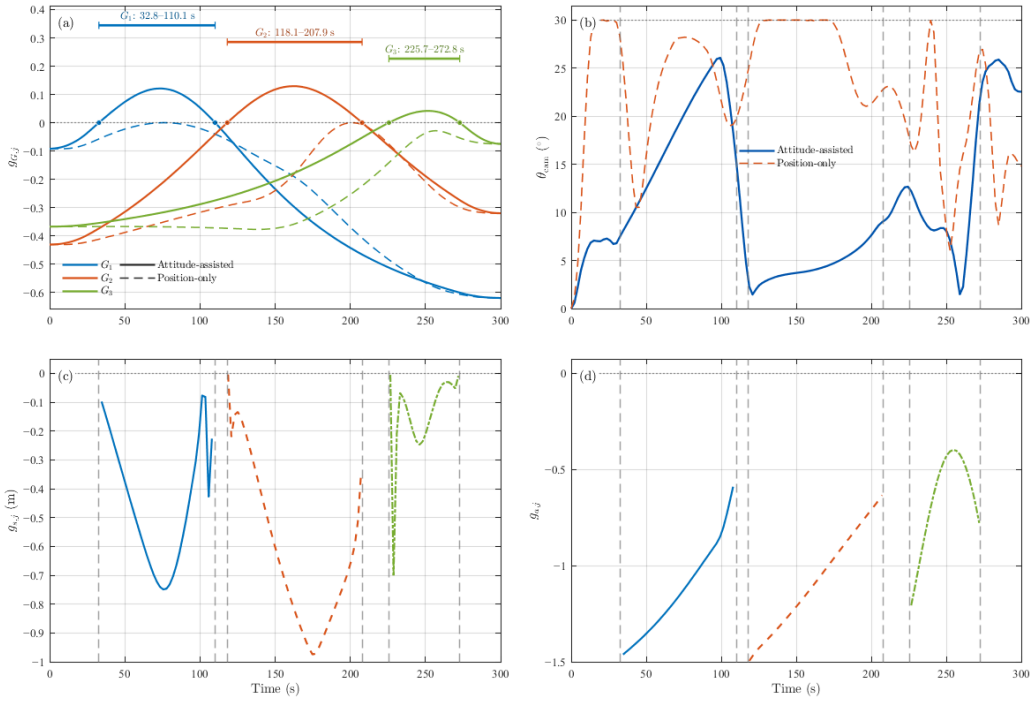


Figure 6. Nodal a posteriori evaluation of the original nonlinear constraints in the main case: (**a**) FOV functions $g_{G,j}$ of the third-party observing spacecraft; (**b**) camera off-axis angle; (**c**) solar-array blocking residual $g_{s,j}$ at FOV-active nodes; and (**d**) rear-aperture residual $g_{a,j}$ at FOV-active nodes. The observer colors follow the legend in (**a**). Gray vertical dashed lines mark FOV-active interval boundaries, while horizontal dotted lines indicate zero-residual constraint boundaries.

Figure 7b shows the two-norm of the attitude control torque. The control torque integrals of the two schemes are 1.3387 N m s and 2.5673 N m s, respectively, with the attitude-assisted scheme reducing this quantity by 47.86%. This result does not imply that

the FOV-avoidance scheme requires no attitude maneuvers. Because the main thrust is strictly aligned with $+x_B$ and the forward camera must also maintain target imaging, the FOV-avoidance scheme likewise requires continuous spacecraft-attitude adjustment to redirect the thrust while generating its pronounced detour trajectory. Consequently, the larger translational detour also requires additional control effort.

Figure 7c shows the evolution of $\|\boldsymbol{\omega}_{BI}^{B}\|_2$, and both schemes satisfy the maximum-angular-velocity constraint at the transcription nodes. Together with Figure 6, these results show that, with identical dynamics, actuator bounds, objective weights, discretization, initialization, and SCvx settings, the attitude-assisted formulation reduces the need for positional detours by exploiting the additional attitude-dependent observation geometry available within third-party FOVs.

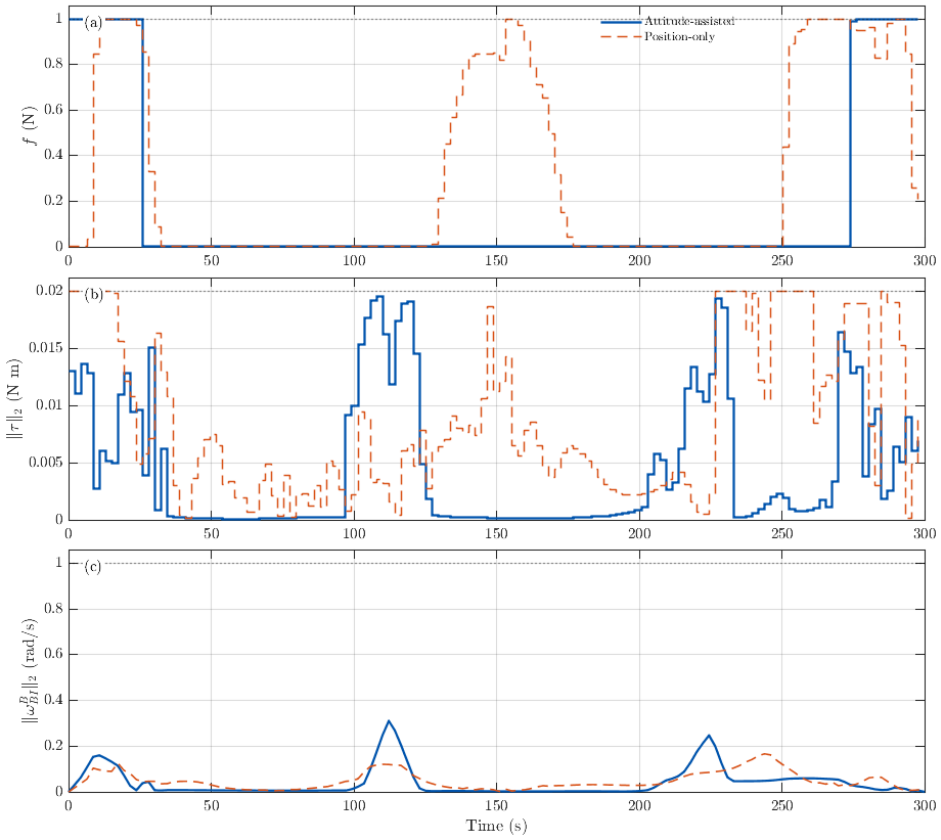


Figure 7. Control and attitude-motion histories of the two mission schemes in the main case: (**a**) unidirectional main-thrust magnitude f; (**b**) control torque norm $\|\boldsymbol{\tau}\|_2$; and (**c**) angular velocity norm $\|\boldsymbol{\omega}_{BI}^{B}\|_2$.

Table 3 summarizes the results of the two schemes. The attitude-assisted and FOV-avoidance schemes meet the relative merit-function-change termination condition after the 18th and 42nd iterations, respectively. The final virtual-control L_1 norms are 3.55×10^{-9} and 1.51×10^{-9} for the attitude-assisted and FOV-avoidance formulations, respectively, while the corresponding aggregate path-slack residual magnitudes are 4.63×10^{-8} and 5.03×10^{-8}. These quantities are numerically negligible, indicating that the artificial feasibility-restoration variables have effectively vanished in the final solutions.

Table 3. Comparison of the two mission schemes in the main case.

Metric	Attitude-Assisted Scheme	FOV-Avoidance Scheme
FOV-active nodes	99 (35/42/22)	0
Thrust impulse (N s)	51.7662	94.7195
Control torque integral (N m s)	1.3387	2.5673
Path length (m)	116.1609	125.2180

4.3. Mission Feasibility Under Unavoidable Observation Conditions

To illustrate the role of attitude freedom when pure FOV avoidance is incompatible with the prescribed terminal geometry, this subsection adjusts the viewing axis of spacecraft G_3 to point directly toward the terminal position $\boldsymbol{r}_f$, while retaining all other settings of the main case. In this case, $g_{G,3}(\boldsymbol{r}_f) = 0.1339746 > 0$, i.e., the terminal position lies inside the field of view of G_3. Therefore, the requirement of the FOV-avoidance formulation to remain outside all observation FOVs throughout the mission conflicts directly with the prescribed terminal boundary and is geometrically infeasible by construction.

The attitude-assisted formulation permits the servicing spacecraft to enter third-party FOVs and uses attitude adjustment to satisfy the prescribed direction-dependent geometric constraints at the corresponding FOV-active transcription nodes. Figure 8 shows the optimized trajectory in this scenario, together with the $+x_B$ and $-z_B$ directions at selected discrete nodes. The resulting discrete solution reaches the prescribed terminal position along a relatively direct trajectory.

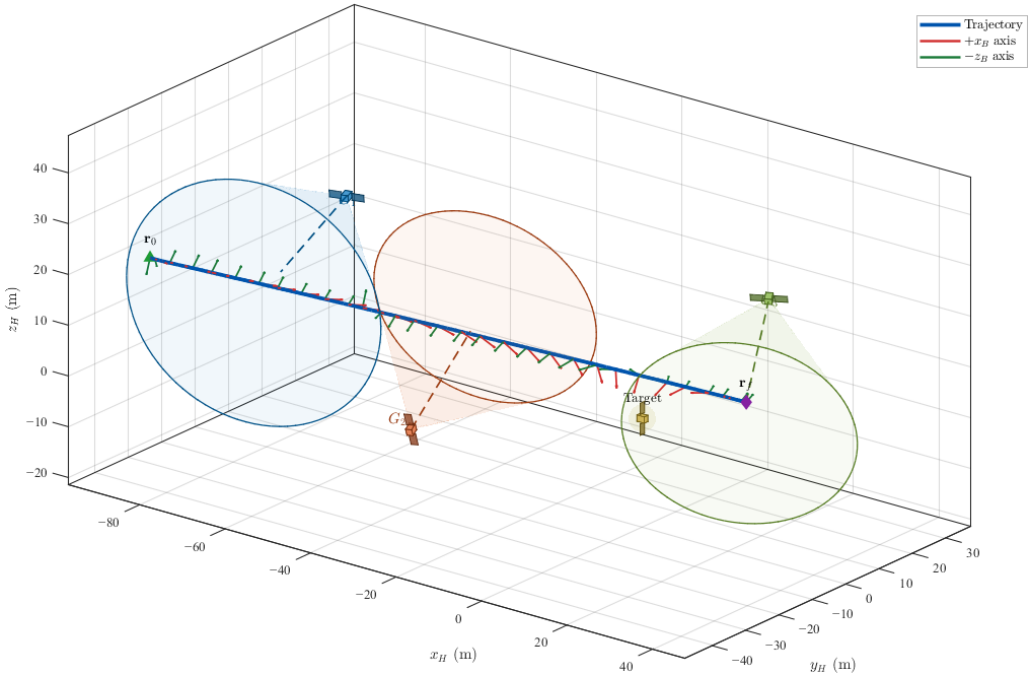


Figure 8. Three-dimensional optimized trajectory and attitude evolution of the attitude-assisted scheme under unavoidable observation conditions.

Figure 9 presents the nodal a posteriori evaluation of the original nonlinear constraints for this trajectory. Figure 9a shows that the servicing spacecraft enters the three third-party FOVs in sequence, with 35, 42, and 23 FOV-active nodes, respectively, for a total of 100 FOV-active nodes. Unlike in the main case, the FOV function of G_3 remains positive at the terminal time, consistent with the preceding analysis of the terminal geometry. Figure 9b shows that all camera off-axis angles remain below the 30° upper bound, with a maximum value of 27.6091°. Thus, while performing attitude adjustments to satisfy the prescribed

geometry-based low-detectability conditions with respect to the third-party observers, the servicing spacecraft can still keep the target within the field of view of the forward-looking optical camera. Over all FOV-active nodes, the maximum solar-array blocking residual in Figure 9c is $\max g_{s,j} = -3.758 \times 10^{-3}$ m. The maximum rear-aperture residual in Figure 9d is $\max g_{a,j} = -0.3891$. $g_{s,j}$ approaches its constraint boundary at several nodes, indicating that when terminal observation is unavoidable, the solar-array blocking constraint plays an active role in constraining the optimal attitude solution.

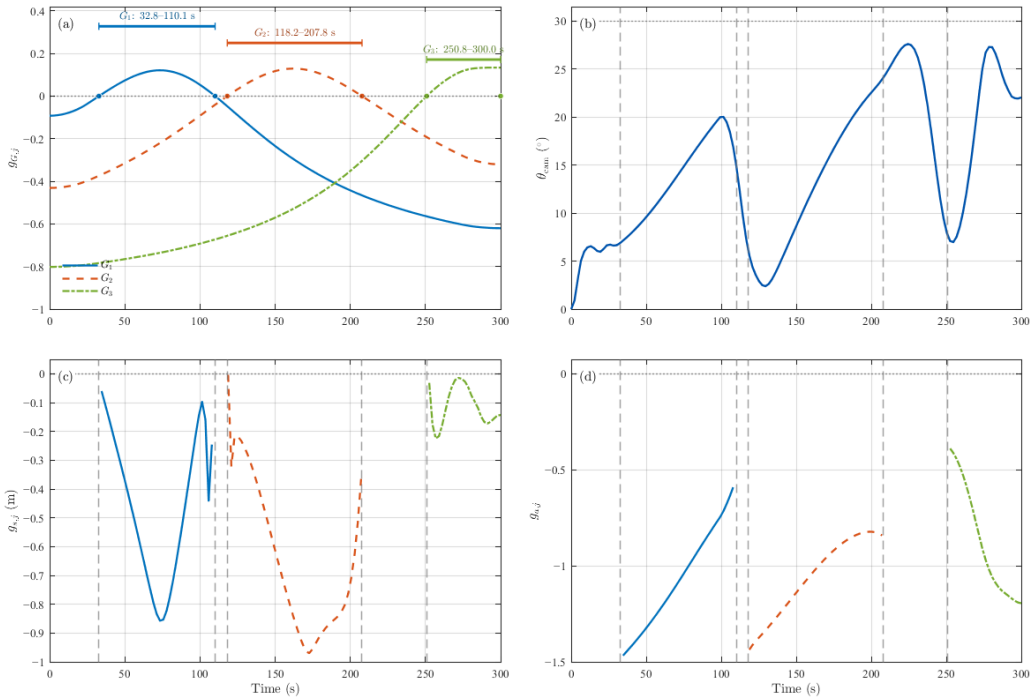


Figure 9. A posteriori evaluation of the original nonlinear constraints for the attitude-assisted formulation under unavoidable observation conditions: (**a**) FOV functions $g_{G,j}$ of the third-party observing spacecraft; (**b**) target-camera off-axis angle; (**c**) solar-array blocking residual $g_{s,j}$ at FOV-active transcription nodes; and (**d**) rear-aperture residual $g_{a,j}$ at FOV-active transcription nodes.

Because the conditional low-detectability constraints are enforced at discrete transcription nodes, satisfaction at the FOV-active nodes does not by itself provide a rigorous guarantee of inter-sample feasibility. In particular, when two adjacent nodes lie on opposite sides of an observation-FOV boundary, the conditional constraint may be inactive at the outside node, although a portion of the continuous trajectory between the two nodes still lies inside the FOV. Consequently, localized inter-sample violations may occur near FOV switching boundaries. The present results should therefore be interpreted as demonstrating constraint satisfaction at the transcription nodes rather than strict continuous-time feasibility. More rigorous treatment of inter-sample constraint satisfaction, for example, through adaptive mesh refinement, interval-level constraints, or conservative trigger margins, is left for future work.

This attitude-assisted scheme satisfies the algorithmic convergence condition after the 18th iteration. Its thrust impulse is 51.7428 N s, its control torque integral is 0.9592 N m s, and its path length is 116.1591 m. Table 4 summarizes the results for this scenario.

Table 4. Transcription-node feasibility results under unavoidable observation conditions.

Metric	Attitude-Assisted Scheme	FOV-Avoidance Scheme
Transcription-node feasibility	Feasible	Geometrically infeasible
FOV-active nodes	100 (35/42/23)	N/A
Maximum camera off-axis angle	27.6091°	N/A
Maximum $g_{s,j}$ (m)	-3.758×10^{-3}	N/A
Maximum $g_{a,j}$	-0.3891	N/A
Thrust impulse (N s)	51.7428	N/A
Control torque integral (N m s)	0.9592	N/A
Path length (m)	116.1591	N/A

These results illustrate a specific terminal-covered geometry in which the FOV-avoidance formulation is infeasible by construction because the prescribed terminal point lies inside a third-party observation FOV. In contrast, the attitude-assisted formulation admits a discrete solution by allowing FOV penetration and exploiting attitude freedom to satisfy the prescribed direction-dependent geometric conditions at the transcription nodes. This example therefore demonstrates additional mission-design freedom provided by attitude assistance with the particular geometry considered here, rather than constituting a complete characterization of feasible-region expansion. As discussed above, the present node-based transcription does not provide a rigorous guarantee of inter-sample satisfaction of the conditional geometric constraints near FOV switching boundaries.

5. Conclusions

This paper investigated 6-DOF joint attitude–trajectory optimization for geometry-based low-detectability spacecraft proximity operations under multiple third-party observation constraints. A coupled attitude–trajectory model was established by jointly considering the forward-looking camera, rear propulsion aperture, direction-dependent solar-array geometric blocking, and body-fixed main thrust. The conditional geometric requirements activated inside third-party observation FOVs were formulated as compound state-triggered constraints (cSTCs) and incorporated into an SCvx-based optimal control framework.

In the main scenario, all FOV-active transcription nodes of the attitude-assisted solution satisfy the prescribed rear-aperture and solar-array blocking constraints. Compared with the FOV-avoidance formulation, the attitude-assisted formulation reduces the thrust impulse from 94.7195 N s to 51.7662 N s, corresponding to a 45.35% reduction in the considered case, while also reducing the need for positional detours. In the terminal-covered scenario, where pure FOV avoidance is incompatible with the prescribed terminal geometry, the attitude-assisted formulation still admits a discrete solution by exploiting attitude freedom to satisfy the direction-dependent geometric requirements at the transcription nodes. These results illustrate the additional mission-design flexibility provided by attitude assistance in multi-observer proximity operations.

The present study uses geometry-based low-detectability surrogates, prescribed observer geometry, CW relative-motion dynamics, and discrete transcription. Therefore, the reported performance should be interpreted within the considered mission scenarios. Future work will consider higher-fidelity signature and orbital-dynamics models, as well as improved treatment of inter-sample constraint satisfaction.

Author Contributions: Conceptualization, J.L. and S.L.; methodology, J.L.; software, J.L. and C.Z.; validation, J.L., C.Z. and B.N.; formal analysis, J.L. and B.N.; investigation, J.L. and C.Z.; resources, S.L.; writing—original draft preparation, J.L.; writing—review and editing, J.L., C.Z. and S.L.; visu-

alization, J.L. and B.N.; supervision, S.L.; project administration, S.L.; funding acquisition, S.L. All authors have read and agreed to the published version of the manuscript.

Funding: This research received no external funding.

Data Availability Statement: Data supporting results are included in the manuscript.

Conflicts of Interest: The authors declare no conflicts of interest.

References

1. Hu, Y.; Li, K.; Liang, Y.; Chen, L. Review on strategies of space-based optical space situational awareness. *J. Syst. Eng. Electron.* **2021**, *32*, 1152–1166. [CrossRef]
2. Zheng, Z.; Bai, Y.; Chen, Z.; Dong, M.; Zhao, Y.; Chen, X. Spacecraft covert maneuvering: Concepts, principles and methods. *J. Astronaut.* **2024**, *45*, 1065–1077. (In Chinese) [CrossRef]
3. Wang, J.; Bai, Y.; Chen, Z.; Zheng, Z.; Zhao, Y.; Chen, X. Covert maneuver trajectory planning of spacecraft cluster based on geodesic. *J. Astronaut.* **2024**, *45*, 513–522. (In Chinese) [CrossRef]
4. Tang, Z.; Zeng, F.; Wang, W.; Li, S. Affine geodesic-based trajectory planning for spacecraft swarm covert maneuver. *J. Guid. Control Dyn.* **2026**, *49*, 618–627. [CrossRef]
5. Zheng, Z.; Bai, Y.; Chen, R.; Zhou, H.; Zhao, Y.; Liu, J. A covert maneuvering trajectory planning method for spacecraft formation based on field of view constraint of surveillance satellite. *Chin. Space Sci. Technol.* **2025**, *45*, 71–83. (In Chinese) [CrossRef]
6. Hu, H.; Zhang, X.; Liao, W.; Kong, X. Research progress and development trend of satellite stealth technology. *J. Natl. Univ. Def. Technol.* **2021**, *43*, 107–127. (In Chinese) [CrossRef]
7. Qin, Y.; Sun, H.; Yue, X. Stealthy configuration design and optimization analysis of microsatellite. *J. Beijing Univ. Aeronaut. Astronaut.* **2022**, *48*, 2102–2110. (In Chinese) [CrossRef]
8. Sun, H.; Qin, Y. Stealthy configuration optimization design and RCS characteristics study of microsatellite. *Aerospace* **2022**, *9*, 815. [CrossRef]
9. Lu, X.; Huang, J.; Wu, Y.; Song, L. Influence of stealth aircraft dynamic RCS peak on radar detection probability. *Chin. J. Aeronaut.* **2023**, *36*, 137–145. [CrossRef]
10. Guan, J.; Song, L.; Wang, H.; Huang, J.; Lu, X. Mechanism analysis and strategies for high-RCS sector avoidance in stealth aircraft during turning maneuvers. *Chin. J. Aeronaut.* **2026**, *39*, 104175. [CrossRef]
11. Su, K.; Zhou, J. Flight attitude planning for low observable micro-satellite shields. *Acta Aeronaut. Astronaut. Sin.* **2011**, *32*, 720–728. (In Chinese)
12. Hua, B.; Liu, R.P.; Wu, Y.H.; Xu, D.F. Intelligent attitude planning algorithm based on the characteristics of low radar cross section characteristics of microsatellites under complex constraints. *Proc. Inst. Mech. Eng. Part G J. Aerosp. Eng.* **2019**, *233*, 4–21. [CrossRef]
13. Li, X.; Wei, Z.; Chen, T.; Zhang, A.; Kong, L. Path Planning and Control of Attitude Maneuver of Flexible Spacecraft on SO(3). *Aerosp. Sci. Technol.* **2026**, *178*, 113057. [CrossRef]
14. Chen, Y.; He, Z.; Zhou, D.; Yu, Z.; Li, S. Integrated guidance and control for microsatellite real-time automated proximity operations. *Acta Astronaut.* **2018**, *148*, 175–185. [CrossRef]
15. Wei, Z.; Yang, J.; Wen, H.; Jin, D.; Chen, T. Nonlinear Optimal Control for Spacecraft Rendezvous and Docking Using Symplectic Numerical Method. *Actuators* **2025**, *14*, 75. [CrossRef]
16. Malyuta, D.; Reynolds, T.P.; Szmuk, M.; Lew, T.; Bonalli, R.; Pavone, M.; Açıkmeşe, B. Convex optimization for trajectory generation: A tutorial on generating dynamically feasible trajectories reliably and efficiently. *IEEE Control Syst. Mag.* **2022**, *42*, 40–113. [CrossRef]
17. Liu, X.; Lu, P. Solving nonconvex optimal control problems by convex optimization. *J. Guid. Control Dyn.* **2014**, *37*, 750–765. [CrossRef]
18. Mao, Y.; Szmuk, M.; Açıkmeşe, B. Successive convexification of non-convex optimal control problems and its convergence properties. In Proceedings of the 2016 IEEE 55th Conference on Decision and Control (CDC), Las Vegas, NV, USA, 12–14 December 2016; pp. 3636–3641. [CrossRef]
19. Mao, Y.; Dueri, D.; Szmuk, M.; Açıkmeşe, B. Successive convexification of non-convex optimal control problems with state constraints. *IFAC-PapersOnLine* **2017**, *50*, 4063–4069. [CrossRef]
20. Zhou, D.; Zhang, Y.; Li, S. Receding horizon guidance and control using sequential convex programming for spacecraft 6-DOF close proximity. *Aerosp. Sci. Technol.* **2019**, *87*, 459–477. [CrossRef]
21. Zhang, Y.; Zhu, B.; Cheng, M.; Li, S. Trajectory optimization for spacecraft autonomous rendezvous and docking with compound state-triggered constraints. *Aerosp. Sci. Technol.* **2022**, *127*, 107733. [CrossRef]
22. Richelson, J.T. Satellite in the shadows. *Bull. At. Sci.* **2005**, *61*, 26–33. [CrossRef]

23. Zheng, K. Research on the Key Technology of Stealthy Microsatellite Structure Design. Ph.D. Thesis, Nanjing University of Aeronautics and Astronautics, Nanjing, China, 2011. (In Chinese)
24. Clohessy, W.H.; Wiltshire, R.S. Terminal guidance system for satellite rendezvous. *J. Aerosp. Sci.* **1960**, *27*, 653–658. [CrossRef]
25. Markley, F.L.; Crassidis, J.L. *Fundamentals of Spacecraft Attitude Determination and Control*; Springer: New York, NY, USA, 2014. [CrossRef]

Disclaimer/Publisher's Note: The statements, opinions and data contained in all publications are solely those of the individual author(s) and contributor(s) and not of MDPI and/or the editor(s). MDPI and/or the editor(s) disclaim responsibility for any injury to people or property resulting from any ideas, methods, instructions or products referred to in the content.